© 2021. Published by The Company of Biologists Ltd | Development (2021) 148, dev196048. doi:10.1242/dev.196048

RESEARCH ARTICLE

Androgen action in cell fate and communication during prostate development at single-cell resolution

Dong-Hoon Lee[1,*], Adam W. Olson[1,*], Jinhui Wang[2], Won Kyung Kim[1], Jiaqi Mi[1], Hong Zeng[3], Vien Le[1], Joseph Aldahl[1], Alex Hiroto[1], Xiwei Wu[2] and Zijie Sun[1,‡]

ABSTRACT

Androgens/androgen receptor (AR)-mediated signaling pathways are essential for prostate development, morphogenesis and regeneration. Specifically, stromal AR signaling has been shown to be essential for prostatic initiation. However, the molecular mechanisms underlying AR-initiated mesenchymal-epithelial interactions in prostate development remain unclear. Here, using a newly generated mouse model, we have directly addressed the fate and role of genetically marked AR-expressing cells during embryonic prostate development. Androgen signaling-initiated signaling pathways were identified in mesenchymal niche populations at single-cell transcriptomic resolution. The dynamic cell-signaling networks regulated by stromal AR were additionally characterized in relation to prostatic epithelial bud formation. Pseudotime analyses further revealed the differentiation trajectory and fate of AR-expressing cells in both prostatic mesenchymal and epithelial cell populations. Specifically, the cellular properties of *Zeb1*-expressing progenitors were assessed. Selective deletion of AR signaling in a subpopulation of mesenchymal rather than epithelial cells dysregulated the expression of the master regulators and significantly impaired prostatic bud formation. These data provide novel, high-resolution evidence demonstrating the important role of mesenchymal androgen signaling in the cellular niche controlling prostate early development by initiating dynamic mesenchyme-epithelia cell interactions.

KEY WORDS: Androgen signaling, Prostate development, Wnt signaling, Sonic hedgehog signaling, Mouse models

INTRODUCTION

The prostate develops from the endodermal urogenital sinus (UGS) that is derived from the caudal terminus of the hindgut called the cloaca (Cunha et al., 2018). Androgen signaling mediated through the androgen receptor (AR) is essential for prostate development (Gelmann, 2002). Mouse prostatic development initiates at embryonic day 17.5 (E17.5) from the UGS in response to rising levels of fetal testicular androgens (Cunha et al., 1987; Staack et al., 2003). Mutation of the *Ar* gene in testicular feminized (Tfm) mice results in the complete absence of prostate development (Cunha and Chung, 1981). During embryogenesis, the AR is initially detected in the urogenital sinus mesenchyme (UGM) before the initiation of prostate budding and morphogenesis. Subsequently, its expression extends to the urogenital sinus epithelium (UGE) after the initiation of prostatic budding and branching morphogenesis (Cunha et al., 1987; Cooke et al., 1991; Takeda and Chang, 1991). Tissue recombination studies further demonstrated that mesenchymal, rather than epithelial, AR signaling plays a decisive role in inducing development of the prostatic epithelium through paracrine regulation (Cunha and Lung, 1978; Cunha, 1984). However, the cellular properties of AR-expressing cells and the mechanisms by which stromal androgen signaling initiates and regulates other pathways and regulators, through mesenchymal-epithelial interactions during early prostatic development and morphogenesis, remain unclear.

During early development, budding and branching morphogenesis takes place in a variety of organs, including the prostate (Ochoa-Espinosa and Affolter, 2012; Iber and Menshykau, 2013; Varner and Nelson, 2014). Despite biological differences in cellular branch structure and function between organs and species, the developmental programs are largely conserved and are regulated by precise spatiotemporal epithelial-mesenchymal paracrine interactions (Thomson et al., 2002; Prins and Putz, 2008). Therefore, investigating mesenchymal androgen action in regulating prostatic budding and development will provide new and important insight into our understanding of cellular niches in branched organ development and their related human disorders.

The AR is a member of the nuclear hormone receptor superfamily (Chang et al., 1988). Androgen-induced AR transcriptional activity directly contributes to early prostate development and morphogenesis (Jenster et al., 1991). To trace AR-expressing cells and assess their functions during prostate development, we used gene-targeting approaches to generate a mouse $Ar^{IRES\text{-}Cre}$ allele, which enables us to genetically mark AR-expressing cells and trace their fate and function in early prostate development. Using single-cell mRNA sequencing (scRNAseq) and other experimental approaches, we evaluated the cellular properties of AR-expressing cells at single-cell resolution, and characterized the signaling pathways and factors that contribute to early prostatic development and morphogenesis in mouse UGS tissues. Trajectory analysis further explores the identity of prostatic progenitors and the regulatory role of AR in prostatic differentiation. These data provide novel, high-resolution insight into cell fates and cell-cell interactions between prostatic mesenchyme and epithelium in early prostate development.

RESULTS

Genetically labeling AR-expressing cells using $Ar^{IRES\text{-}Cre}$ mice

Using gene targeting approaches, we generated a new mouse model, $Ar^{IRES\text{-}Cre}$ mice, by inserting *Cre* recombinase into the mouse *Ar* gene locus on the X chromosome through an engineering internal ribosome entry site (IRES) within the 3′ untranslated region

[1]Department of Cancer Biology, Cancer Center and Beckman Research Institute, City of Hope, Duarte, CA 91010, USA. [2]Integrative Genomics Core, Cancer Center and Beckman Research Institute, City of Hope, Duarte, CA 91010, USA. [3]Transgenic, Knockout and Tumor Model Center, Stanford University School of Medicine, Stanford, CA 94305, USA.
*These authors contributed equally to this work

‡Author for correspondence (zjsun@coh.org)

Z.S., 0000-0002-6787-6272

Handling Editor: Samantha Morris
Received 14 August 2020; Accepted 30 November 2020

Development (2021) 148, dev196048. doi:10.1242/dev.196048

(Fig. 1A). This advanced mouse tool allows for *Ar* promoter-directed expression of *Cre* recombinase while maintaining endogenous *Ar* expression. Both male and female $Ar^{IRES\text{-}Cre}$ mice, including both heterozygotes and homozygotes, were viable and fertile, and presented no visible abnormalities. Female $Ar^{IRES\text{-}Cre/X}$ mice were then crossed with male $Rosa26^{mTmG/+}$ ($R26R^{mTmG/+}$) reporter strains to generate $R26R^{mTmG/+}$:$Ar^{IRES\text{-}Cre/Y}$ mice (Fig. 1B). The activity of *Cre* recombinase results in spontaneous recombination of the *floxed* reporter loci, generating a permanent genetic marker by switching from expression of membrane-bound tandem dimer Tomato (mT) to membrane-bound green fluorescent protein (mGFP) (Muzumdar et al., 2007) (Fig. 1B). Those genetically labeled cells will not only carry mGFP expression through their lifespan but will also pass it to their offspring, enabling us to trace the fate of AR-expressing cells and descendants.

Histological analysis of adjacent UGS sections prepared from male $R26R^{mTmG/+}$:$Ar^{IRES\text{-}Cre}$ embryos between the ages of E12.5 and E17.5 showed normal morphology of the UGS at each time point (Fig. 1C1-C6). Co-staining of UGS tissues for vimentin, a mesenchymal cellular marker, and E-cadherin, an epithelial marker, visually separated epithelial and mesenchymal compartments in these sections (Fig. 1D1-D6). Interestingly, *Cre*-induced mGFP expression first appears mainly within the UGE in E12.5 UGS tissues (Fig. 1E1). The expression of mGFP continues to increase in the UGE and, starting at E13.5, is gradually revealed in the adjacent UGM (Fig. 1E2). The observation of mGFP expression in the UGE prior to that in the UGM is unexpected and suggests that *Ar* transcription actually occurs first in UGE cells, differing from the results reported previously (Cunha et al., 1987; Cooke et al., 1991; Takeda and Chang, 1991). Although the UGE appears almost completely mGFP positive by E14.5 and beyond, cells located in the protruding Wolffian duct remain mT positive through E17.5 (Fig. 1E5-G6, blue arrows). Immunofluorescent staining for mGFP showed a similar expression pattern to that observed in mTmG assays at different time points (Fig. 1F1-F6). Relatively weak AR staining appears within the UGM and beyond the UGE areas starting at E12.5 (Fig. 1G1,I1). It gradually becomes stronger (Fig. 1G2,G3) and extends to UGE areas, clearly visualized at E14.5 in both the UGE and UGM (Fig. 1G4-G6). At E12.5 and E13.5, cytoplasmic staining of AR appeared in cells with mGFP and DAPI (Fig. 1I1,I2,J1,J2, white arrows). However, uniform nuclear staining of AR clearly overlaps with DAPI in mGFP-positive UGE and UGM cells of E14.5 and elder UGS samples (Fig. 1I3-I6,J3-J6). The above results showed that *Cre*-induced mGFP expression mimics the expression pattern of endogenous AR but appears stronger than AR expression in UGS tissues. Additionally, the observation of mGFP prior to AR expression in UGE areas at E12.5 suggests that different translation processes through the 5′ cap and the IRES site take place for AR and *Cre* protein synthesis, respectively (Komar and Hatzoglou, 2011). Nevertheless, the current $R26R^{mTmG/+}$:$Ar^{IRES\text{-}Cre}$ model provides a new tool for detecting and tracing AR-expressing cells.

Assessing urogenital sinus cell populations using single-cell RNA sequencing

To assess the characteristics of AR-expressing cells in early prostate development, we performed single-cell RNA sequencing (scRNAseq) analyses using UGS tissues isolated from male $R26R^{mTmG/+}$:$Ar^{IRES\text{-}Cre}$ embryos (Fig. 2A). At E17.5, UGE and immediately surrounding mesenchyme reveal positive staining for *Ar-Cre*-induced mGFP expression, whereas much of the more distant stroma is mT positive, especially closer to the bladder (Fig. 2B). In addition, the Wolffian duct epithelial cells and their surrounding stromal cells, remain mT positive (blue arrow, Fig. 2B). Embryonic UGS tissues were dissected, and non UGS tissues, including the Wolffian duct, bladder and urethra, were removed (Fig. 2C); ∼11,000 viable cells were collected and used for sequencing with 10× Genomics Chromium Single Cell 3′ Solution (Fig. 2A). Following sequencing and alignment to the mm10 reference genome with an added mGFP sequence (Chen et al., 2015), 10,478 cells were included after the initial quality control in the analysis using the Seurat package (Butler et al., 2018). Cells then underwent filtering to remove potential empty droplets, doublets and low-quality cells with high percentages of mitochondrial RNA. After this final filtering step, 9440 cells with an average of 4976 genes and 31,214 UMI counts per cell were used for future analyses (Fig. S1A,B). When visualized in two dimensions based on unbiased transcription profiling using t-Distributed Stochastic Neighbor Embedding (tSNE), 21 distinct cellular clusters were identified (Fig. 2D). The cellular properties of these clusters were assessed using mesenchymal and epithelial cellular markers, including smooth muscle actin (*Acta2*), vimentin (*Vim*) and epithelial cell adhesion molecule (*Epcam*) (Fig. 2E and Fig. S2). Based on their expression patterns, epithelial and mesenchymal cell populations were determined and grouped (Fig. 2F). Seven stromal and four epithelial cell types were further identified (Fig. 2G-I) based on their transcription profiles in comparison with previously reported urogenital cellular markers and scRNAseq datasets from mouse and human prostate tissues (Georgas et al., 2015; Cunha et al., 2018; Henry et al., 2018; Kwon et al., 2019). Five highly expressed genes representing specific cellular properties in each cluster were shown (Fig. 2I). Based on these cellular markers, four epithelial clusters were identified as urogenital sinus epithelial (UGE), bladder epithelial (BLE), Wolffian duct epithelial (WDE), and other epithelial (OE) cells. Most of the epithelial cells were in the UGE cluster with high expression of *Krt15*, *Krt4* and *Tspan1*. These UGE cells also showed higher expression of *Ar* and *mGFP* compared with other epithelial cells (Fig. S2). The cells in the BLE cluster displayed high expression of *Upk3a*, *Upk2* and *Sptssb*, typical bladder cellular markers (Georgas et al., 2015; Habuka et al., 2015) (Fig. 2I), and low expression of *Ar* and *mGFP* compared with the UGE. The expression of *Pax8*, *Pax2*, and *Hoxb7*, WDE cell markers, was present in the WDE cluster (Narlis et al., 2007; Georgas et al., 2015) (Fig. 2B, Fig. S2A). Observation of small BLE and WDE cell clusters in the above samples was expected as those tissues cannot be completely removed from the UGS during sample preparation. Last, the OE cell cluster contains about 60 cells with high expression of *Lrrn4*, *Gpm6a* and *Muc16*, suggesting they have mesothelial cell properties (Kanamori-Katayama et al., 2011).

Seven stromal cell types were identified in the analysis. Most of the stromal cells possess fibroblast properties with *Dcn*, *Fbln1* and *Gsn* expression (Guerrero-Juarez et al., 2019; Karpus et al., 2019). Smooth muscle cells are the second largest stromal cell population featuring high expression of *Acta2*, *Tagln* and *Myh11* (Brun et al., 2015). Other minor stromal clusters were identified as leukocytes (Henry et al., 2018), endothelial cells (Fontijn et al., 2014), peripheral glial cells and neurons (Jessen and Mirsky, 2005; Jacob et al., 2014), and myoblasts (Ganassi et al., 2018), representing a similar cellular composition of the UGS at this timepoint, as reported previously (Georgas et al., 2015). Among those stromal clusters, *Ar* and *mGFP* are highly expressed in fibroblasts, with some limited expression in smooth muscle cells (Fig. 2I and Fig. S2A). These data provide a comprehensive landscape of the cell populations and properties of the male embryonic urogenital sinus at single-cell resolution.

Development (2021) 148, dev196048. doi:10.1242/dev.196048

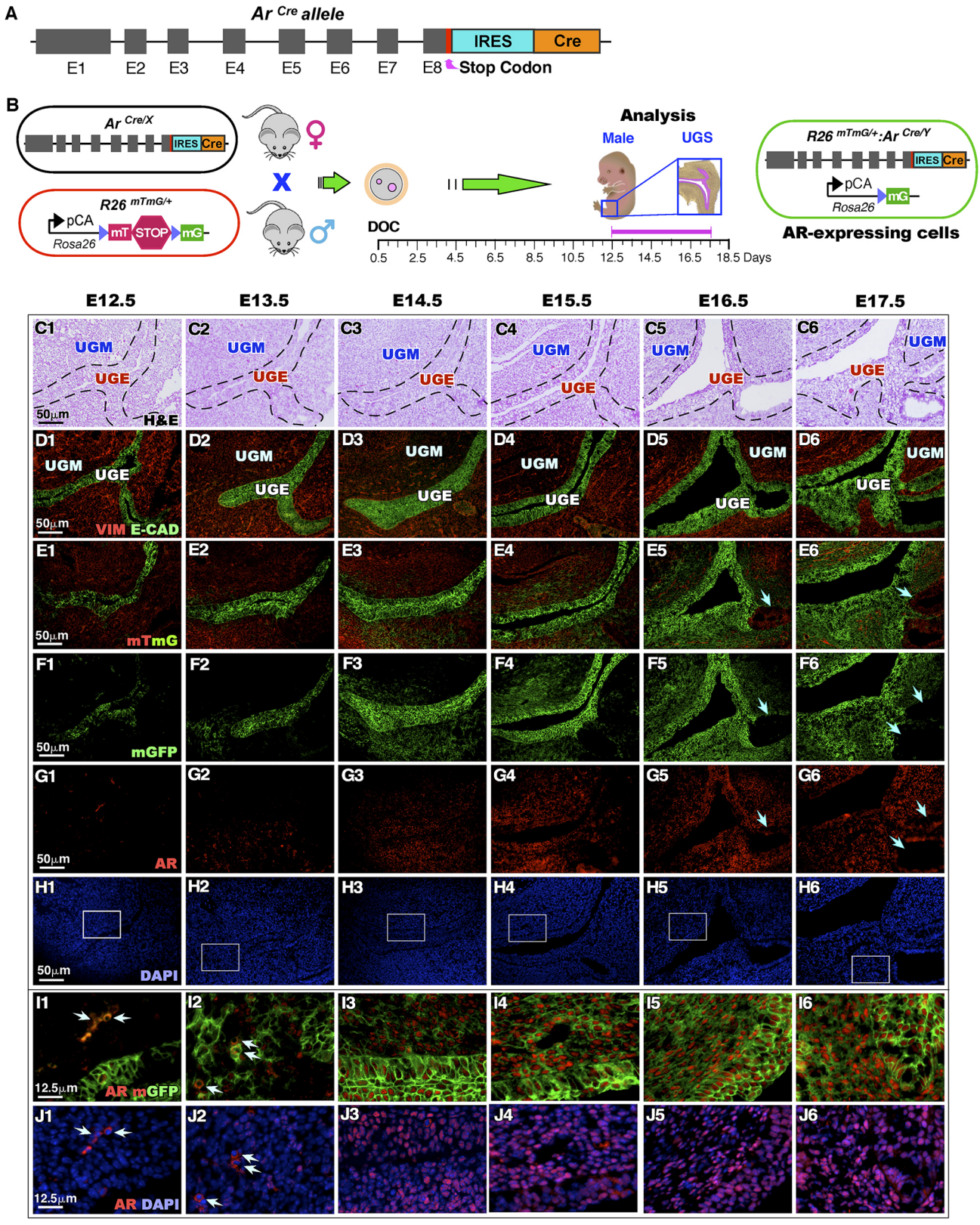

Fig. 1. Generation and characterization of *Ar*$^{IRES\text{-}Cre}$ mice. (A) Genetic construct of the targeted *Ar* allele displaying the inserted IRES and Cre sequences. (B) Schematics of the *Ar*$^{IRES\text{-}Cre}$ and *R26*$^{mTmG/+}$ alleles are shown in relation to the mating strategy for this experiment. Following the day of conception (DOC), a timeline is provided indicating the days of analysis as shown. A construct is displayed demonstrating the recombination event that will take place in *Ar*-expressing cells, resulting in a change from red to green fluorescence. (C) A total of four UGS samples at each time point were isolated and analyzed in this and other figures. Representative Hematoxylin and Eosin images are displayed with dashed lines separating urogenital sinus epithelium and mesenchyme at the indicated time points. (D-J) Representative fluorescence imaging for the indicated proteins/antibodies. Blue arrows in images indicate mT-positive Wolffian duct structures (E5,E6,F5,F6,G5,G6). White arrows indicate cytoplasmic staining for AR outside the nucleus (I1,I2,J1,J2).

Development (2021) 148, dev196048. doi:10.1242/dev.196048

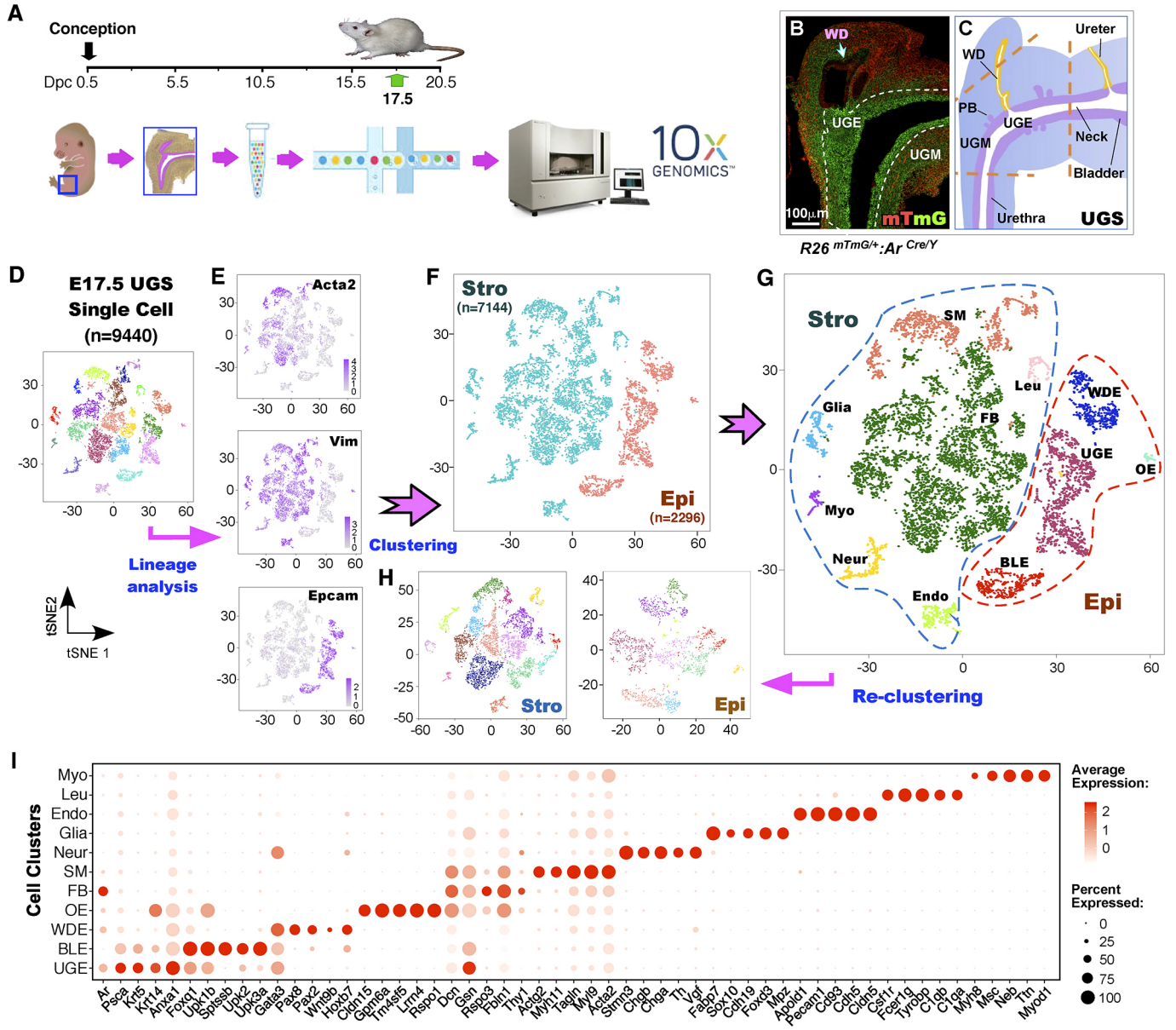

Fig. 2. Single-cell RNA sequencing of E17.5 male mouse UGS. (A) The timeline of the single-cell sequencing experiment performed. (B) A representative mTmG assay image of a cross-section of a *R26*$^{mTmG/+}$*:Ar*$^{IRES\text{-}Cre}$ male UGS. The mT-positive Wolffian duct epithelium is marked with a blue arrow. (C) An illustration depicting a male E17.5 UGS indicates, with dashed orange lines, roughly how the samples were trimmed prior to single-cell sequencing (PB, prostatic bud). (D) A tSNE plot of single cells isolated from four male E17.5 urogenital sinuses. (E) Gene expression tSNE plots for the indicated epithelial and stromal cell marker genes. (F) Original clustering results grouped into either epithelial or stromal (non-epithelial) groups. (G) Identification of cell types, as indicated within the original clustering results. (H) Two tSNE plots show re-clustering results after separating the stromal and epithelial cell groups. (I) A dot plot of *Ar* and groups of five genes highly specific to each cell type identified.

Characterization of AR signaling in both urogenital epithelial and stromal cells

Using the transcription profiles generated with scRNAseq, we further assessed the expression of endogenous *Ar* and *Cre*-induced *mGFP* at single-cell resolution in embryonic UGS tissues at E17.5. Most AR-expressing cells appear in the fibroblast and UGE cell clusters, and the signals from the former appear more intense than those from the latter (Fig. 3A-C). *Cre*-induced *mGFP* expression also appeared in both fibroblast and UGE cell clusters (Fig. 3B,C). The level of *mGFP* expression between the fibroblast and UGE cell clusters is comparable and is, in both cases, stronger than that of endogenous *Ar* (Fig. 3B,C). The different expression pattern between *mGFP* and endogenous *Ar* may be attributed to the fact that their transcription is regulated under different promoters, following the initial *Cre*-mediated activation of *mGFP* (Muzumdar et al., 2007). Analysis of cell distributions showed almost half of stromal and epithelial cells being *mGFP* and *Ar* positive (Fig. 3D). However, about one-quarter of stromal and one-third of epithelial cells appeared only *mGFP* positive, reflecting the transient nature of *Ar* expression in early prostate development. Few cells showed *Ar* expression without mGFP expression, suggesting *Ar* expression may have just initiated in those cells. Finally, about one-quarter of cells showed no detection of either *Ar* or *mGFP* expression in both the stroma and epithelia (Fig. 3D). Using immunofluorescent approaches, we validated the expression of endogenous AR and mGFP, as well as other cell markers in UGS tissues. AR and mGFP

Development (2021) 148, dev196048. doi:10.1242/dev.196048

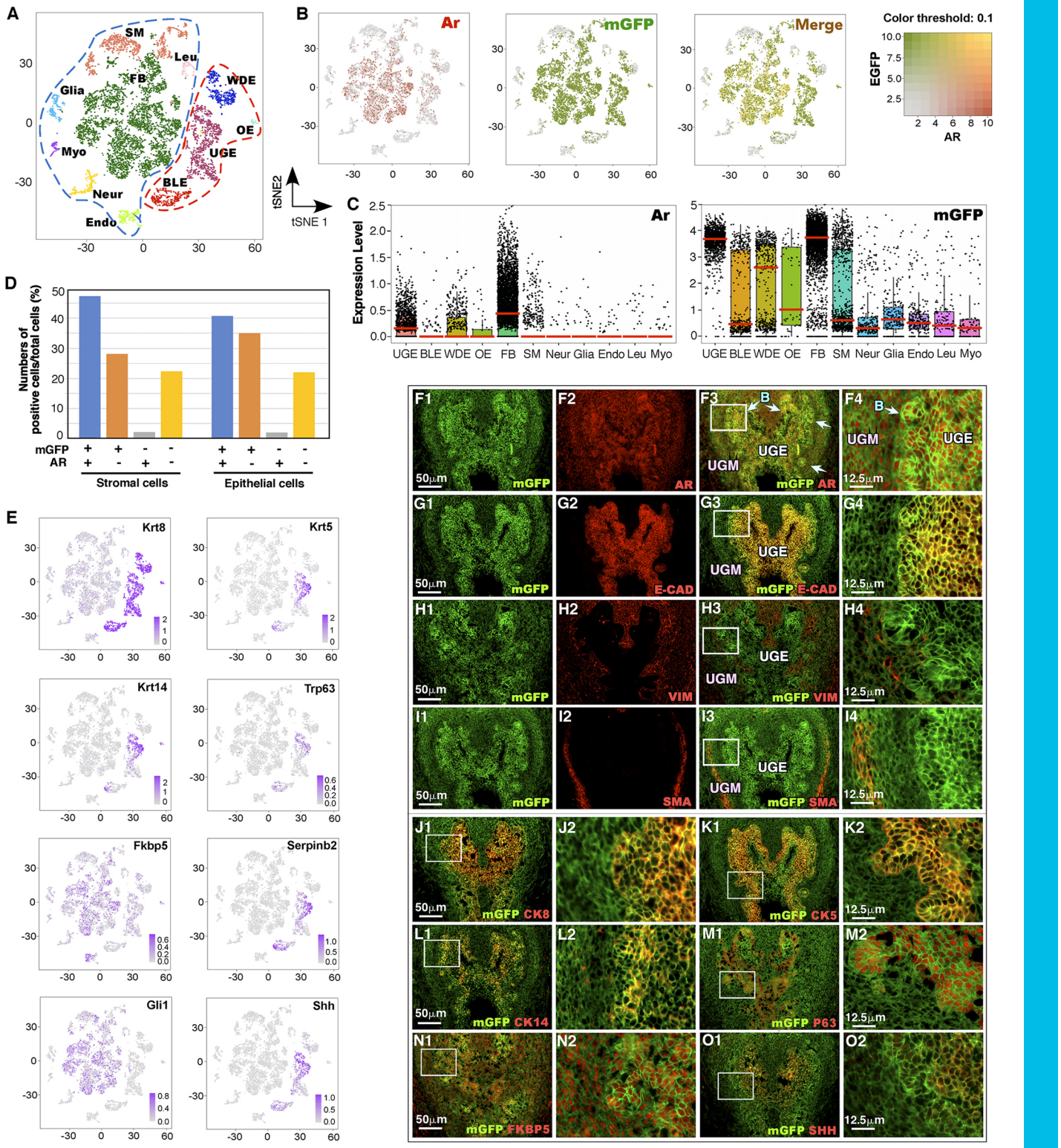

Fig. 3. Characterization of *Ar*-expressing cells using scRNAseq. (A) tSNE plot of overall UGS tissue. (B) Blended tSNE expression plots displaying cell clusters with expression of *Ar* and *mGFP*. (C) Box plots representing scaled expression data for *Ar* and *mGFP*. Red lines mark the median expression value. (D) Bar chart corresponding to the percentage of stromal and epithelial cells with *Ar* and *mGFP* expression, as indicated. (E) Gene expression tSNE plots displaying expression patterns of the indicated genes. (F-O) Representative co-immunofluorescence images of male E17.5 UGS tissue stained for the indicated antibodies. Blue arrows indicate prostatic buds (F3,F4). F4,G4,H4,I4,J2,K2,L2,M2,N2 and O2 depict high-magnification images corresponding to the boxed regions of F3,G3,H3,I3,J1,K1,L1,M1,N1 and O1, respectively.

double-positive cells appear in both the UGE and UGM areas (Fig. 3F1-F4). Interestingly, staining for mGFP in the UGE cells appears stronger than UGM cells (Fig. 3F1). AR and mGFP double-positive cells also make up prostatic buds (arrows, Fig. 3F3,F4). The majority of UGE cells appear uniformly positive for E-cadherin and mGFP; however, weaker E-cadherin staining is present in areas

Development (2021) 148, dev196048. doi:10.1242/dev.196048

along the exterior epithelial layer, especially the protruding prostatic buds (Fig. 3G1-G4). Co-staining of mGFP with vimentin was observed in the stromal cells directly surrounding the UGE cells (Fig. 3H1-H4). Smooth muscle cells appear to be separated from the UGE by several layers of fibroblasts and exhibit limited overlap with mGFP (Grishina et al., 2005) (Fig. 3I1-I4). The above co-immunofluorescence results provide *in situ* expression patterns in support of the previous scRNAseq transcription profile analyses.

The cellular properties of urogenital epithelial and mesenchymal cells were further evaluated using both scRNAseq and immunostaining. *Krt8*, a luminal epithelial marker appears to be expressed uniformly throughout epithelial cell clusters (Fig. 3E), supported by relatively uniform positive staining for CK8 within the UGE (Fig. 3J1,J2). *Krt5*, *Krt14* and *Trp63*, prostatic basal cell markers, are localized to only the upper part of the UGE cluster in tSNE expression plots (Fig. 3E), and showed positive staining localized to the outer basal layer of the UGE and the prostatic buds (Fig. 3E,K1,K2,L1,L2,M1,M2). Staining of mGFP was also present in UGS areas and was overlaid with the above cellular markers. Interestingly, the expression of *Fkbp5* and *Serpinb2*, two AR downstream target genes, showed different patterns. The expression of *Fkbp5* appears in both mesenchymal and epithelial cells (Fig. 3E,N1,N2), whereas *Serpinb2* is mainly expressed within the urogenital and bladder epithelial cells. Sonic hedgehog (Shh) is mainly present in the UGE and bladder cell clusters, whereas *Gli1*, a downstream target gene of Shh, appears in fibroblasts and smooth muscle cells (Fig. 3E), implicating their reciprocal regulation in early prostate development (Podlasek et al., 1999). Positive staining for Shh was also observed in the UGE cells (Fig. 3O1,O2). The above results from both tSNE expression and co-immunofluorescence staining provide new and consistent insight into the cellular properties of AR-expressing cells in embryonic UGS tissues.

High-resolution single-cell profiling of urogenital sinus epithelial cells

To assess androgen signaling-initiated paracrine interactions between prostatic epithelial and mesenchymal cells, the epithelial cells were grouped and re-clustered, again yielding UGE, BLE, WDE and OE

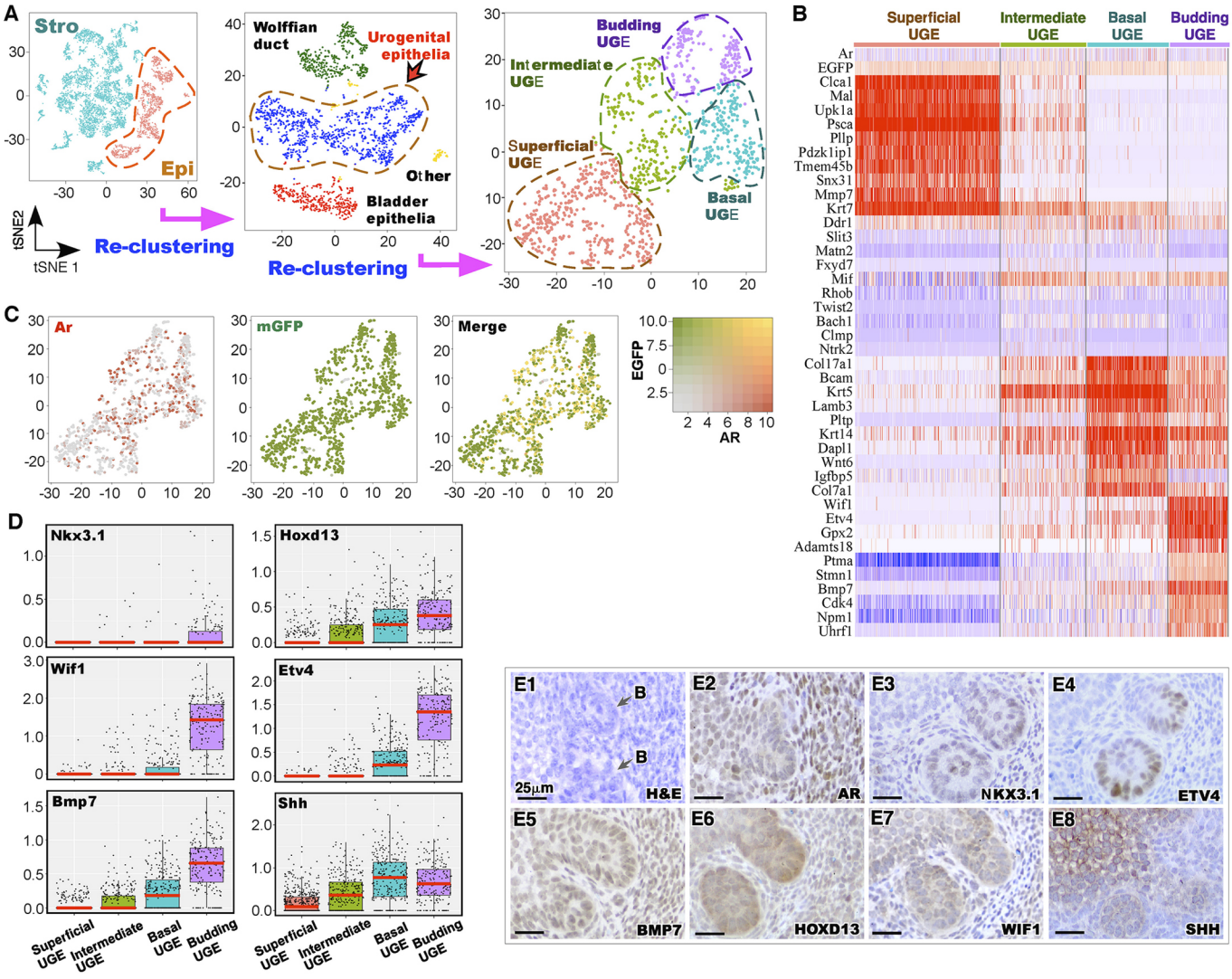

Fig. 4. Single-cell RNA sequencing analysis of the urogenital sinus epithelium. (A) tSNE plots showing the separation and re-clustering of UGE cells. (B) Heatmap of the top 10 differentially expressed genes for each of the four UGE clusters. (C) Blended expression tSNE plots of *Ar* and *mGFP* expression in the UGE. (D) Box plots depicting scaled gene expression of the indicated genes. Red lines mark the median expression value. Boxes indicate the boundaries of the first and third quartiles. The top and bottom whiskers indicate the maximum and minimum expression values, respectively, excluding outliers. (E) Representative Hematoxylin and Eosin, and immunohistochemistry images of prostatic buds stained for the indicated proteins. Prostatic buds are indicated with arrows in E1.

Development (2021) 148, dev196048. doi:10.1242/dev.196048

cell clusters (Fig. 4A and Fig. S3A-C). Given the biological significance of UGE cells in prostate development, we further re-clustered these cells. Re-clustering resulted in four clusters that were identified from the innermost to the outermost layer of the UGE, including superficial, intermediate, basal and budding UGE clusters based on urogenital epithelial cellular markers (Bhatia-Gaur et al., 1999; Grishina et al., 2005; Abler et al., 2011; Keil et al., 2012) (Fig. 4A,B and Fig. S3D,E). Although nearly all cells within these clusters are *mGFP* positive, levels of *Ar* expression vary, with the highest expression in the basal and intermediate UGE (Fig. 4C). Expression of prostatic budding markers, such as *Nkx3.1*, *Wif1* and *Bmp7*, were mainly localized to the budding UGE cells, as well as *Shh* and *Hoxd13*, a transcription regulator involved in prostatic differentiation (Javed and Langley, 2014) (Fig. 4D). Interestingly, *Etv4*, which interacts with Shh and Fgf signaling in branching morphogenesis (Lu et al., 2009; Herriges et al., 2015; Zhang et al., 2016), was also highly expressed in the budding UGE cells. A full list of DEGs specific to the budding UGE was generated (Table S1). Immunohistochemistry analysis showed AR expression in both UGM and UGE areas, but weaker expression presented in budding epithelial cells than in adjacent stromal cells (Fig. 4E1,E2). Nkx3.1 and Etv4 expression appears selectively in the budding epithelial cells (Fig. 4E3,E4), whereas the expression of Bmp7, Hoxd13 and Wif1 was seen in both budding epithelial and surrounding stromal cells (Fig. 4E5-E7). Interestingly, staining for Shh appears noticeably weaker in the budding epithelial cells than in adjacent basal UGE cells (Fig. 4E8). A similar staining pattern has been observed in an earlier study (Podlasek et al., 1999). These data provide a clear breakdown of UGE cells at single-cell resolution during the onset of prostatic bud formation.

Trajectory analysis of urogenital epithelial differentiation

To explore the differentiation patterns of UGE cells, we performed trajectory analysis using Monocle's reverse graph embedding (Qiu et al., 2017). Three well-defined branches with budding UGE and superficial UGE cells concentrated at two opposing branch tips were generated with Monocle analysis. Basal and intermediate UGE cells made up most of the central region of the plot, displaying an overall arch from the innermost to the outermost UGE cell types (Fig. 5A,B). A mixture of basal and intermediate UGE cells formed the third, shorter branch tip (Fig. 5A). Prostatic basal cells, particularly, *Zeb1*-expressing basal cells, are thought to possess stem/progenitor cell properties and the ability to differentiate to prostatic luminal cells (Toivanen et al., 2016; Wang et al., 2020). Consistent with this recent study (Wang et al., 2020), the expression of *Zeb1* appears to be concentrated at the end of the basal and intermediate UGE branch in the trajectory plot (Fig. 5C). Therefore, in the pseudotime plot, the point of origin was set as the small basal/intermediate branch displaying focal *Zeb1* expression (Fig. 5B,C). This group of *Zeb1* expressing cells also showed focal expression of other EMT related genes (Fig. 5C,D). A list of DEGs specific to this cell population was identified (Table S2). From that population, two distinct differentiation paths leading to prostatic bud cells and superficial UGE were revealed (Fig. 5B,C). These differentiation paths similarly start with a reduction in EMT markers, although the budding epithelial cells display a slight recovery of EMT-related genes, possibly contributing to their increased motility (Fig. 5D, right panel). *Nkx3.1, Etv4* and *Wif1* expression appears to be concentrated at the budding UGE branch tip (Fig. 5C,D). Although slightly diffuse, *Hoxd13* and *Bmp7* showed strongest expression in the budding UGE (Fig. 5C,D). These data suggest a regulatory role for *Etv4*, *Wif1* and *Nkx3.1* in differentiated budding cells while *Hoxd13* and *Bmp7* may act in initiating basal UGE cell differentiation to prostatic buds (Fig. 5C,D). Co-immunofluorescnece staining showed clear nuclear staining of ZEB1 in the majority of UGM cells; however, only varying cytoplasmic staining in UGE cells (Fig. 5E1, E5). Epithelial ZEB1 staining was also overlaid slightly with CK8 but not Trp63 staining in UGE cells (arrows, Fig. 5E4,E5,E7,E8). The above observations appear similar to previous reports showing cytoplasmic staining of ZEB1 in epithelial cells (Spaderna et al., 2006; Goscinski et al., 2015). Using SCENIC upstream regulator analysis (Aibar et al., 2017), we further assessed the driving factors contributing to UGE cell differentiation (Fig. S3F). The top 20 transcription factors (TFs) were identified in each UGE cell type, including Wnt (Sp5 and Tcf7) and Notch signaling-related regulators (Zfp64 and Hey1), as well as ETV family members (Fig. S3F). Taken together, these data determine the differentiation status of UGE cells and explore the cell properties of urogenital epithelial progenitor cells at single-cell resolution.

Characterizing cellular properties of urogenital sinus mesenchymal cells

We similarly re-clustered the stromal cells to gain deeper insight into their cell characteristics (Fig. 6A). Eight cell types were identified (Fig. 6B). The newly identified cell type, pericytes, were previously grouped within the smooth muscle cells (Fig. 2G). High expression of *Ar* and *mGFP* appeared primarily in fibroblasts (Fig. S4C). As urogenital sinus fibroblasts are directly adjacent to the UGE and involved in regulating the epithelial-mesenchymal paracrine interactions during early prostate development (Grishina et al., 2005; Abler et al., 2011), we re-clustered them to further characterize their cellular properties. Of the nine resulting clusters, one showed high expression levels of cell proliferation-related genes (Fig. 6C). Using cell-cycle regression, we removed those genes from the principal component analysis (PCA). Following this regression, re-clustering produced eight fibroblast clusters (Fig. 6D,E) that were grouped into four subtypes, including progenitor-like (ProGf), Col14a1-expressing (Col14a1f), peri-epithelial (PeriEf) and other fibroblasts (OF) (Fig. 6F).

We first identified *Bmp7*-, *Wif1*- and *Wnt5a*-expressing fibroblasts following reports that they are directly surrounding prostatic buds and involved in early prostate development and morphogenesis (Grishina et al., 2005; Huang et al., 2009; Keil et al., 2012). The expression of *Bmp7*, *Wif1* and *Wnt5a* appear mainly in clusters F4 and F5, and thus were identified as peri-epithelial fibroblasts (Fig. 6F,G), which also showed the highest level of *Ar* expression among the fibroblast clusters (Fig. 6F). In co-immunofluorescence analyses, Bmp7, Wif1 and Wnt5a proteins were also detected in the epithelial buds and surrounding stromal cells and overlaid with AR (Fig. 6I′-K′). In addition, as observed in the scRNAseq, staining for AR appeared strongest in the UGM adjacent to the UGE, whereas the lowest expression levels were observed in the prostatic buds (Fig. 6I′-K′). The expression of Bmp7, Wif1, and Wnt5a along with elevated AR appeared in peri-epithelial fibroblasts as well as in the budding UGE cells, implicating their participation in epithelial-mesenchymal paracrine interactions during prostatic epithelial budding and development.

We further assessed the relationships between different fibroblast clusters during early prostate development using trajectory analysis. Four major branch tips were observed in the trajectory plot generated using Monocle (Fig. 6H). Their differentiation states were predicted using CytoTrace (Fig. S4D-F). Based on this, a group of potential progenitor fibroblasts, clusters F1 and F2, were identified at one of the branch tips, and set as the starting point for pseudotime analysis (Fig. 6H). The peri-epithelial fibroblasts were

Development (2021) 148, dev196048. doi:10.1242/dev.196048

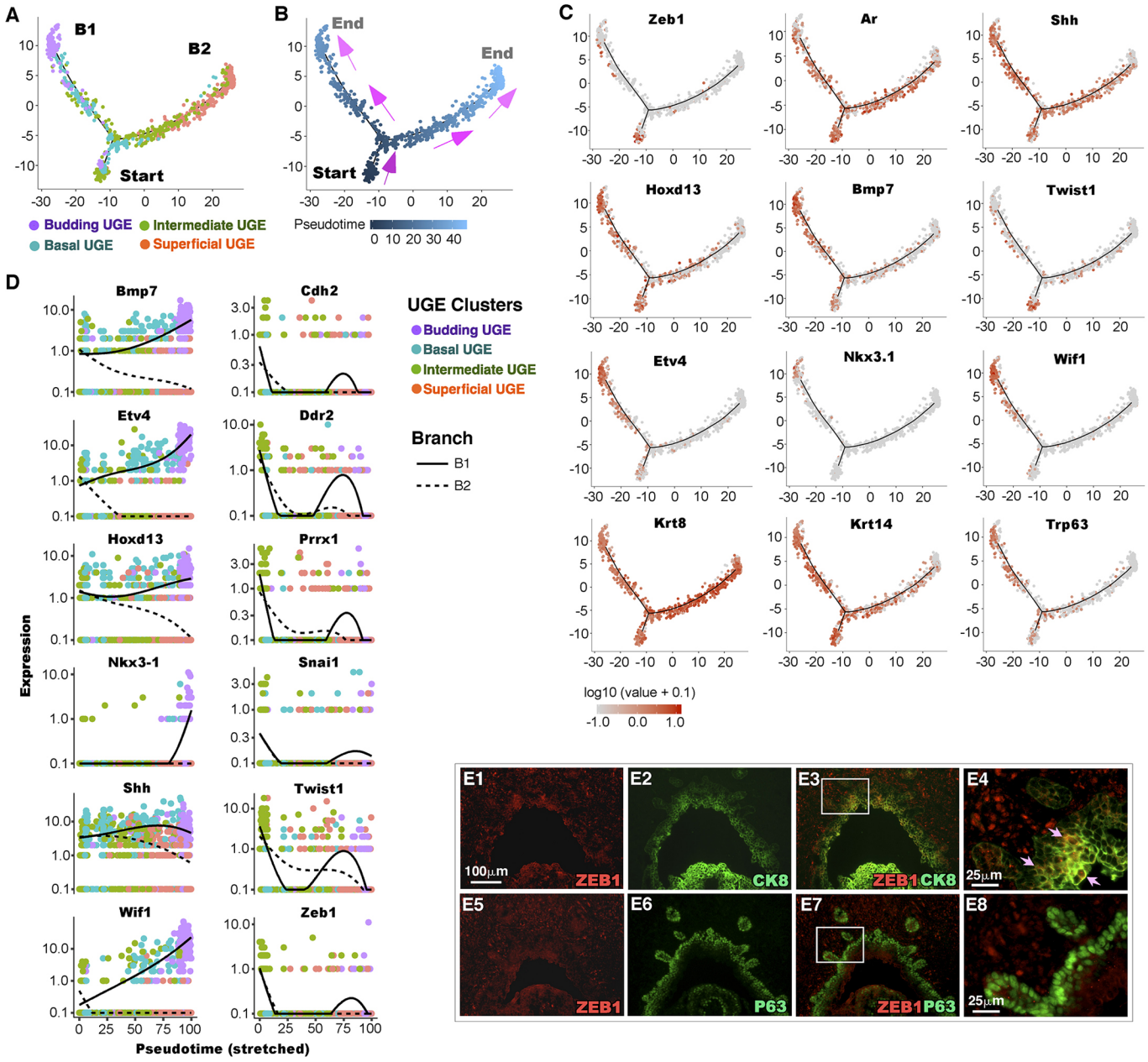

Fig. 5. Trajectory analysis of the urogenital sinus epithelium. (A) Trajectory analysis of UGE single cells. (B) Pseudotime plot displays a predicted directional path of differentiation between cell types as indicated. (C) Expression of the indicated genes in the trajectory plot. (D) Linear pseudotime expression plots for the indicated budding and EMT marker genes. Lines on each plot correspond to the path of differentiation moving from the start point (left) to the indicated branch tip (right). (E) Representative images of immunofluorescent staining for the indicated proteins in E17.5 male UGS tissues. Pink arrows (E4) indicate cytoplasmic epithelial *Zeb1* staining. E4 and E8 depict high-magnification images corresponding to the boxed regions of E3 and E7, respectively.

grouped together at another branch tip (Fig. 6H). A third branch tip featured a group of fibroblasts, primarily from cluster F3, with high expression of *Col14a1*, *Clec3b* and *Anpep* (Fig. 6F,H), similar to Col14a1 expressing fibroblast populations reported in the lung and skin (Xie et al., 2018; Guerrero-Juarez et al., 2019). The identity of the fourth branch tip is unclear and possesses a mixture of the fibroblast subtypes. The expression of *Bmp7* and *Wif1* were mainly observed in the peri-epithelial fibroblast branch tip, while *Wnt5a*, *Fgfr2 Hoxd13* and *Gli1* expression appeared in all fibroblast branch tips but with focal expression on some individual tips (Fig. 6L). These trajectory analyses explored the cellular properties and differentiation status of prostatic fibroblasts.

Identifying molecular mechanisms underlying mesenchymal AR-mediated regulatory pathways during early prostate development

To assess the regulatory role of the peri-epithelial fibroblasts in early prostate development, we examined the DEGs comparing the transcriptomes of peri-epithelial fibroblasts against the other fibroblasts (Fig. 7A and Table S3). Using gene set enrichment analysis (GSEA) with different databases, a number of enriched pathways, previously reported to directly associate with branching morphogenesis, were identified (Fig. 7B), including Wnt/β-catenin, Bmp, hedgehog, androgen and retinoic acid-related signaling pathways. The top 40 DEGs from the above analysis displayed

Development (2021) 148, dev196048. doi:10.1242/dev.196048

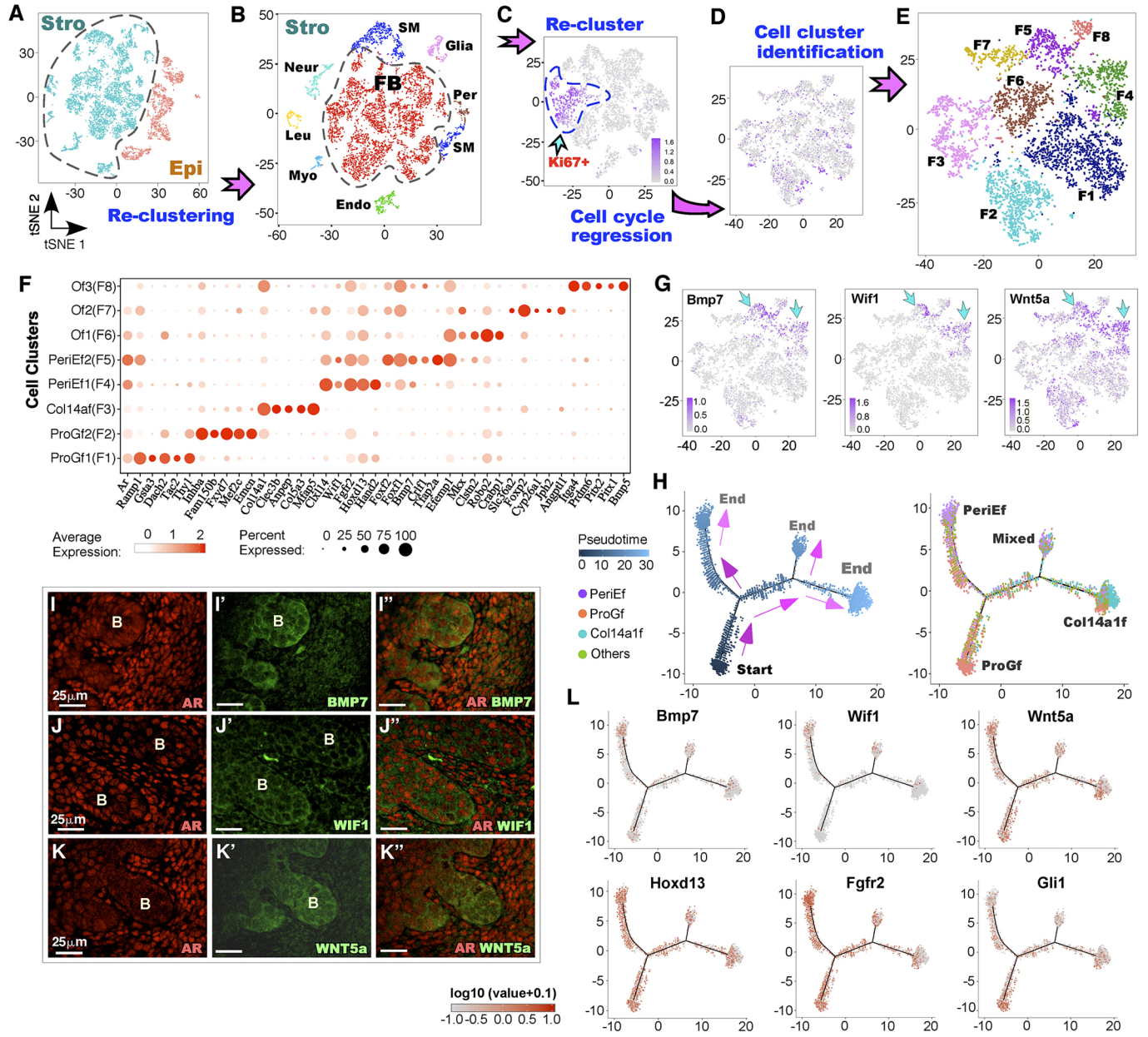

Fig. 6. Single-cell RNA sequencing analysis of the urogenital sinus mesenchyme. (A) tSNE plot showing the stromal cell clusters selected for re-clustering. (B) Stromal re-clustering tSNE plot divided by cell type, as indicated, showing selection of fibroblasts for re-clustering. (C) tSNE plot identifying *Mki67* expression following initial re-clustering of fibroblasts. (D) tSNE plot of *Mki67* expression, following cell cycle regression. (E) tSNE plot of final fibroblast clustering results used for analysis. (F) A dot plot of *Ar* and five genes highly specific to each fibroblast cluster. (G) Expression tSNE plots of the indicated peri-epithelial fibroblast markers. (I-K″) Representative co-immunofluorescence images of male E17.5 UGS sections stained for the indicated antibodies; prostatic buds are marked with 'B'. (H) Trajectory analysis of fibroblast cells. Pseudotime indicates a predicted pathway of differentiation between the fibroblast subtypes, as indicated. (L) Expression plots of the indicated genes in pseudotime.

elevated expression of peri-epithelial fibroblast markers *Wif1, Bmp7* and *Wnt5a*, along with hedgehog downstream targets, *Foxf1*, *Cxcl14* and *Dner* (Madison et al., 2009; Yu et al., 2009), and Wnt downstream targets, *Lef1* and *Tcf4* (Fig. 7A). Using IPA, a subset of upregulated AR downstream genes was identified from the above DEGs, suggesting a regulatory role for AR in peri-epithelial fibroblasts (Fig. 7C). Using chromatin immunoprecipitation-quantitative polymerase chain reaction (ChIP-QPCR), we demonstrated an enrichment in the regulatory regions of AR downstream target genes (Nash et al., 2019), including *Fgfr2*, *Fgf7*, *Sgk1*, *Prkca* and *Ets2* in AR antibody immunoprecipitated DNA samples isolated from E17.5 UGM cells in comparison with input samples (Fig. 7D). The transcriptional regulators enhanced in peri-epithelial fibroblasts were further identified using SCENIC (Aibar et al., 2017) master regulator analysis (Fig. 7E), including seven Fox and Hox family TFs, five Wnt-related TFs, including Lef1 and Tcf4, as well as Sox9 and Sox4. In addition, many of these TFs have been identified as AR-associated proteins and co-regulators (http://androgendb.mcgill.ca/ARinteract.pdf; Fig. 7E). Given proximity of peri-epithelial fibroblasts to the budding UGE cells, we characterized the interactomes between these two clusters to explore the paracrine interactions between the two cell types using SingleCellSignalR methods (Cabello-Aguilar et al., 2020). Predicted ligand-receptor interactions related to Fgf, Tgfβ, Shh, Wnt and Notch signaling pathways appeared in both directions between

Development (2021) 148, dev196048. doi:10.1242/dev.196048

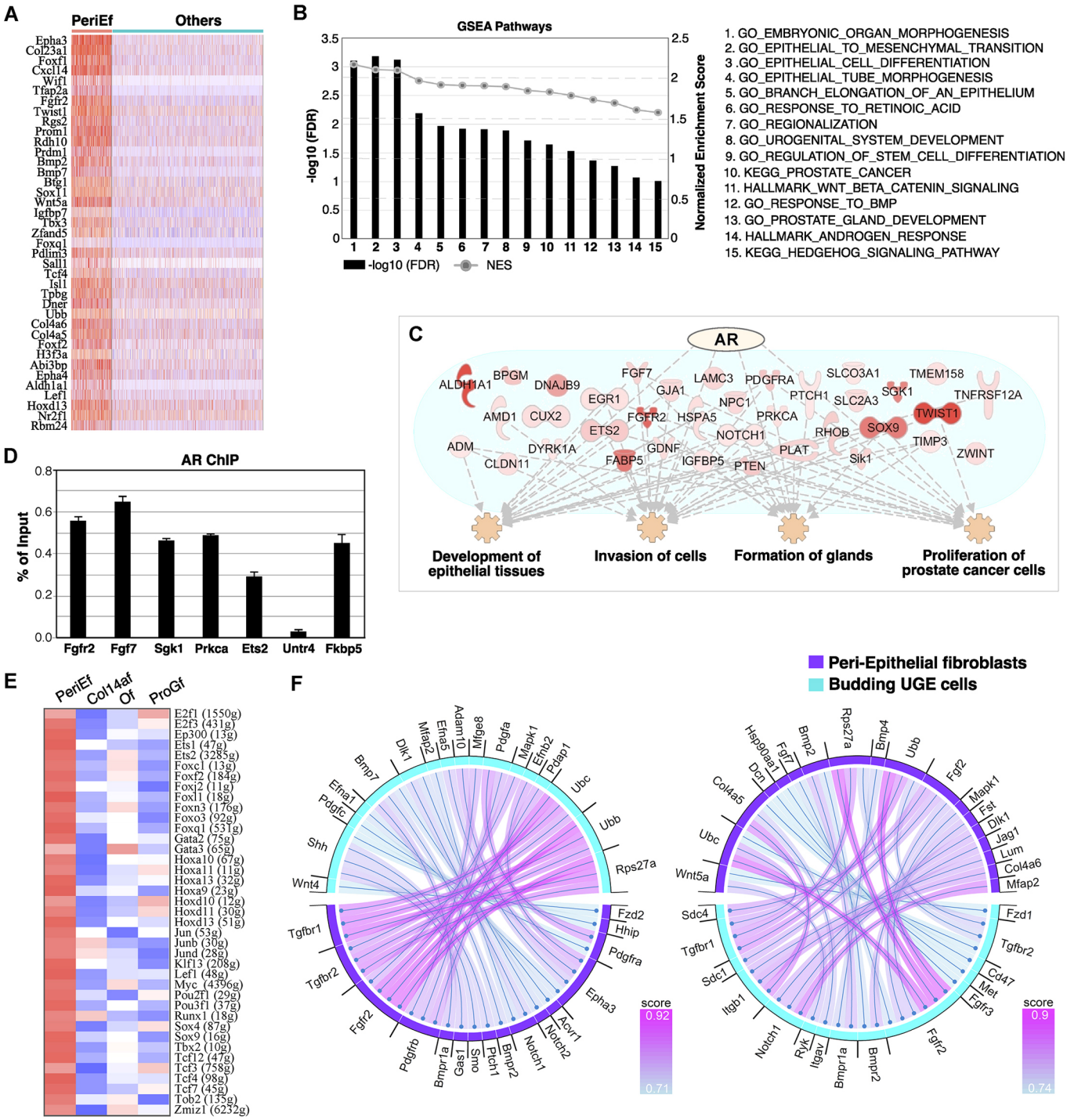

Fig. 7. Identification of potential mechanisms related to peri-epithelial AR signaling. (A) Heatmap of the top 40 differentially expressed genes specific to the peri-epithelial fibroblast clusters. (B) GSEA pathway analysis results comparing the peri-epithelial fibroblast clusters to the remaining fibroblasts. (C) AR downstream targets were identified as being upregulated in peri-epithelial fibroblasts using the upstream regulator analysis of IPA. Enriched pathways related to the AR downstream targets are indicated. (D) ChIP-qPCR analyses were conducted using E17.5 UGM cells. Immunoprecipitated chromatin DNA fragments with AR antibody were analyzed by real-time qPCR with specific primers for the AR downstream target genes as labeled in the figure. (E) Transcription factors with enhanced activity in peri-epithelial fibroblasts relative to the remaining fibroblasts generated using SCENIC upstream regulator analysis. (F) Predicted ligand-receptor interactions between budding UGE cells and peri-epithelial fibroblasts, as indicated, generated using SingleCellSignalR. Color scale corresponds to interaction scores.

peri-epithelial fibroblast and budding UGE cell clusters (Fig. 7F). These data demonstrate the important role of peri-epithelial fibroblasts in inducing prostate epithelial development and provide an atlas for further investigating the role of AR and other regulators in controlling prostate initiation and development.

Deletion of AR in urogenital sinus mesenchymal cells, but not epithelial cells, impairs prostate budding and development

Using mouse genetic tools, we further assessed the role of AR in UGM and UGE cells during early prostate development. As illustrated in Fig. 8A,B, selective deletion of *Ar* expression and activation of mGFP

Development (2021) 148, dev196048. doi:10.1242/dev.196048

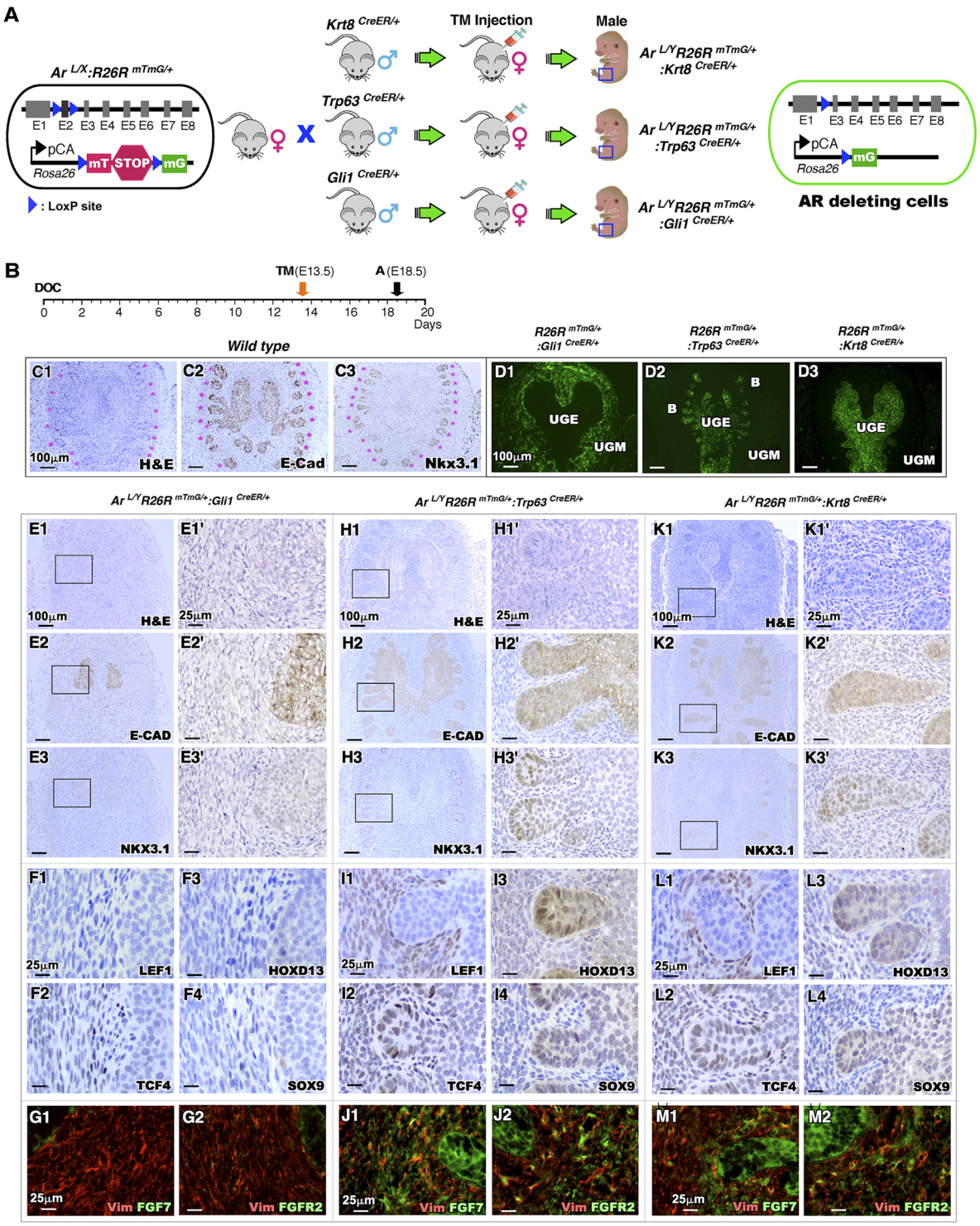

Fig. 8. Effects of selective *Ar* deletion on prostatic budding and expression of key developmental genes. (A) Schematic identifying gene constructs and mating strategies to yield *Cre* promoter-specific *Ar* deletion in the indicated models. (B) Timeline for tamoxifen injection and analysis of tissue samples following day of conception (DOC). (C) Representative Hematoxylin and Eosin, and immunohistochemistry staining images of wild-type E18.5 male urogenital sinuses. (D) Representative fluorescence images of mGFP in male E18.5 urogenital sinus tissues from the indicated genotypes. (E1-G2) Representative images of the indicated staining of male E18.5 $R26R^{mTmG/+}$:$Ar^{L/Y}$:$Gli1^{CreERT2/+}$ UGS tissue. (H1-J2) Representative images of the indicated staining of male E18.5 $R26R^{mTmG/+}$:$Ar^{L/Y}$:$Trp63^{CreERT/+}$ UGS tissue. (K1-M2) Representative images of the indicated staining of male E18.5 $R26R^{mTmG/+}$:$Ar^{L/Y}$:$Krt8^{CreERT2/+}$ UGS tissue. Boxed areas in E1-E3, H1-H3 and K1-K3 are depicted at higher magnification in E1′-E3′, H1′-H3′ and K1′-K3′, respectively.

expression in *Gli1*-expressing cells in the UGM, and in *Trp63*- and *Krt8*-expressing cells in the UGE was achieved by administrating TM at E13.5 in $R26R^{mTmG/+}$:$Ar^{L/Y}$:$Gli1^{CreERT2/+}$, $R26R^{mTmG/+}$:$Ar^{L/Y}$:$Trp63^{CreERT/+}$ and $R26R^{mTmG/+}$:$Ar^{L/Y}$:$Krt8^{CreERT2/+}$ mice, respectively (Fig. 8B). Histological and immunohistochemical analyses showed normal prostate budding with positive staining of E-cadherin

Development (2021) 148, dev196048. doi:10.1242/dev.196048

and Nkx3.1 in UGS tissues isolated from E18.5 wild-type mice (Fig. 8C1-C3). Immunofluorescence staining of mGFP in UGS tissues of *R26R*$^{mTmG/+}$*:Gli1*$^{CreERT2/+}$, *R26R*$^{mTmG/+}$*:Trp63*$^{CreERT/+}$ and *R26R*$^{mTmG/+}$*:Krt8*$^{CreERT2/+}$ mice showed *Gli1*-expressing cells in the UGM, and *Trp63*- and *Krt8*-expressing cells in different UGE compartments (Fig. 8D1-D3), demonstrating their mesenchymal or epithelial properties, respectively. Examining E18.5 UGS tissues of *R26R*$^{mTmG/+}$*:Ar*$^{L/Y}$*:Gli1*$^{CreERT2/+}$ mice revealed no prostatic bud formation (Fig. 8E1-E3′), consistent with previous reports (Le et al., 2020). In contrast, no significant defects appeared in UGS tissues isolated from *Ar*$^{L/Y}$*:R26R*$^{mTmG/+}$*:Trp63*$^{CreERT/+}$ and *Ar*$^{L/Y}$*:R26R*$^{mTmG/+}$*:Krt8*$^{CreERT2/+}$ embryos (Fig. 8H1,H1′,K1,K1′). Positive staining of both E-cadherin and Nkx3.1 also appear in the above UGS tissues (Fig. 8H2,H3′,K2,K3′). These data further demonstrate the significant role of mesenchymal AR signaling in prostate budding and development. Positive staining for Lef1, Tcf4, Hoxd13 and Sox9, which we demonstrated to be enhanced in peri-epithelial fibroblasts (Fig. 7A,C), was observed in the UGM or in both UGM and UGE cells of *Ar*$^{L/Y}$*:R26R*$^{mTmG/+}$*:Trp63*$^{CreERT/+}$ and *Ar*$^{L/Y}$*:R26R*$^{mTmG/+}$*:Krt8*$^{CreERT2/+}$ tissues (Fig. 8I1-I4,L1-L4). Both Fgf7 and Fgfr2 (with VIM co-staining) are also present in *Ar*$^{L/Y}$*:R26R*$^{mTmG/+}$*:Trp63*$^{CreERT/+}$ and *Ar*$^{L/Y}$*:R26R*$^{mTmG/+}$*:Krt8*$^{CreERT2/+}$ UGM cells (Fig. 8J1,J2,M1,M2). However, little to no staining for those proteins was detected in *Ar*$^{L/Y}$*:R26R*$^{mTmG/+}$*:Gli1*$^{CreERT2/+}$ UGS tissues (Fig. 8F1-F4,G1,G2). Taken together, these data demonstrate that selective deletion of AR in mesenchymal *Gli1*-expressing cells, but not in UGE cells, impairs prostatic budding and diminishes the expression of key transcriptional and paracrine regulators in embryonic UGS tissues. This also provides proof-of-principle evidence supporting the scRNAseq data in this study.

DISCUSSION

Currently, the molecular mechanisms underlying fetal androgen-induced interactions with other signaling pathways in early prostate development remain unclear. Specifically, the identity of prostatic AR-expressing cells that convey androgen signaling and control early prostate induction and development are unknown. In this study, using the novel mouse strain *R26R*$^{mTmG/+}$*:Ar*$^{IRES\text{-}Cre/Y}$, we assessed AR-expressing cell properties and investigated the molecular basis of AR-mediated signaling in initiating prostatic mesenchymal-epithelial interactions during early prostate development. Interestingly, *Cre*-induced mGFP expression through endogenous AR transcription appeared in the E12.5 UGE rather than the UGM. This observation provides the experimental evidence that AR transcription actually occurs first in the UGE although the expression of endogenous AR proteins is first detected in the UGM at E13.5 (Cooke et al., 1991). This observation is also consistent with an early *in vivo* hybridization study showing that AR transcription starts at E12.5 in UGE and UGM cells (Crocoll et al., 1998). *Cre*-induced mGFP expression appears to mimic the expression pattern of endogenous AR but in a much more sensitive manner, which may be due to the high efficiency of *Cre*-mediated recombination and the different translational processes between the 5′ cap and IRES site for synthesizing AR and Cre proteins (Komar and Hatzoglou, 2011). Therefore, the *Ar*$^{IRES\text{-}Cre}$ model is a valuable tool for tracing AR-expressing cells when combined with reporter alleles, and for perturbation and manipulation of androgen signaling through the incorporation of other floxed alleles.

Using the *Ar*$^{IRES\text{-}Cre}$ model with scRNAseq and other experimental approaches, we assessed the male E17.5 UGS epithelial and mesenchymal cell types. The expression of endogenous *Ar* and *Cre*-initiated mGFP was mainly observed in the UGE and fibroblast cell clusters, suggesting the biological significance of androgen signaling in these cells. We further separated and re-clustered these cell populations individually to visualize them at the highest resolution. Based on highly specific expression of prostatic budding markers, including *Nkx3.1*, *Wif1* and *Bmp7*, we identified a cluster comprising budding epithelial cells. In addition, the expression of *Etv4*, a key regulator in budding/branching processes in lung and kidney branching morphogenesis (Lu et al., 2009; Costantini, 2010; Herriges et al., 2015) and in promoting epithelial-mesenchymal transition (EMT) and prostate cancer progression (Pellecchia et al., 2012; Aytes et al., 2013), was also identified as a novel marker of budding UGE cells. Using trajectory analysis with Monocle and CytoTrace software, we also explored the cellular identity of prostatic epithelial progenitors in E17.5 UGS tissues. A potential progenitor population comprising *Zeb1*-expressing cells within basal/intermediate UGE clusters was identified, showing opposing pathways of differentiation leading to either budding or superficial UGE clusters (Wang et al., 2020). These results provide new insight into the cellular properties of budding and UGE progenitor cell populations, and provided unbiased characterization of the transcriptomes of these unique epithelial cells, helping to identify the signaling pathways and regulators acting in prostatic epithelial differentiation and development.

We also characterized urogenital stroma to better understand mesenchymal AR signaling in regulating epithelial-mesenchymal paracrine interactions during prostate epithelial development. As urogenital sinus fibroblasts are directly adjacent to the UGE, we specifically focused on peri-epithelial fibroblasts, which were shown to have the highest AR expression and expression of *Bmp7*, *Wif1* and *Wnt5a*, regulators of prostatic budding (Grishina et al., 2005; Huang et al., 2009; Abler et al., 2011). Upregulation of developmental signaling pathways, including Wnt/β-catenin, Bmp, retinoic acid, hedgehog and androgen signaling were identified in these fibroblasts based on the DEGs when compared with other fibroblasts. IPA analyses showed the upregulation of AR downstream target genes in these peri-epithelial fibroblasts. ChIP Q-PCR further demonstrated an enrichment of AR binding in the regulatory regions of AR target genes, reported in AR ChIPseq data from P0 rat ventral and dorsolateral prostate lobes (Nash et al., 2019), in AR-antibody immunoprecipitated E17.5 UGM samples. Analysis of the interactions between the prostatic bud epithelia and peri-epithelial fibroblasts, using SingleCellSignalR (Cabello-Aguilar et al., 2020), further identified paracrine interactions related to Wnt, Bmp, Notch and hedgehog signaling pathways. The above data provide the molecular basis for mesenchymal AR in regulating paracrine interactions between mesenchymal and epithelial cells at single-cell resolution during prostate early development.

Last, using mouse genetic tools, we further evaluated the role of epithelial and mesenchymal AR in prostate development. Consistent with previous reports (Le et al., 2020), impairment of prostatic budding appeared in E17.5 UGS tissues with *Gli1*-CreER-induced *Ar* deletion but no significant defects showed in counterparts with *Krt8*- or *Trp63*-CreER-induced AR deletion, further demonstrating the crucial role of mesenchymal AR in prostate development. Interestingly, *Zeb1* expression was observed mainly in mesenchymal *Gli1*-expressing cells, although epithelial *Zeb1*-expressing cells with co-expression of *Krt8* also showed weak expression of *Gli1* in tSNE plots (Fig. S5A-F). These observations raise the possibility of either *Gli1*-expressing cells as the origin of *Zeb1*-expressing progenitors or Gli1 expression occurring in epithelial cells during embryonic prostate development. Therefore, more effort should be devoted to defining the cellular properties of *Gli1*- and *Zeb1*-expressing cells as prostatic stem cells and/or their niche cells in prostate development. Taken together, this study

Development (2021) 148, dev196048. doi:10.1242/dev.196048

provides significant insight into the regulatory role of mesenchymal AR and provides a wealth of data for future studies of epithelial-mesenchymal interactions in prostatic development and disease.

MATERIALS AND METHODS

Mouse generation, mating and genotyping

All animal procedures were approved by the City of Hope Institutional Animal Care and Use Committee (IACUC). *Rosa26*$^{mTmG/+}$ (*R26*$^{mTmG/+}$) reporter mice were kindly provided by Dr Liqun Luo (Stanford University, CA, USA) (Muzumdar et al., 2007). Experimental mice were generated by intercrossing *Ar*$^{IRES\text{-}Cre/X}$ female mice with *R26*$^{mTmG/+}$ male mice. *Gli1*^{CreER} mice were obtained from Jackson Laboratories (stocks 007913). *Ar*$^{Lox/Y}$ mice were obtained from Dr Guido Verhoeven (De Gendt et al., 2004). *Trp63*^{CreERT2} and *Krt8*^{CreERT2} mice were generated as described previously (Lee et al., 2014; Zhang et al., 2012). To elicit genetic recombination, mice were intraperitoneally injected with 125 µg/g body weight of tamoxifen (TM, Sigma) suspended in corn oil (Sigma) as previously reported (Lee et al., 2015). Genotyping was performed using the primers provided (Table S4). The targeting vectors for generating *Ar*$^{IRES\text{-}Cre}$ mice were designed based on a previous study for making *Ar*$^{IRES\text{-}PLAP\text{-}IRES\text{-}nLacZ}$ mice (Shah et al., 2004). The IRES-Cre fragment was generated using PCR approaches from the IRES-mCherry plasmid (Addgene #80139) and assembled accordingly. The fragment was introduced to the region after the stop codon of the mouse *Ar* gene. Three guide RNAs (gRNA) were designed at the above insertion site, one gRNA (AAGTGCCCAAGATCCTTTCT) was chosen after *in vitro* cutting efficiency validation. The gRNA was synthesized using *in vitro* transcription approaches, and CAS9 protein was purchased from PNA Bio. The above IRES-cre donor DNA fragment (dDNA) was cloned into the targeting vector and bracketed with left and right homologous arms (~1 kb each), which were generated by PCR using C57Bl6/J mouse genomic DNA as template with the following pairs of primers: AR-5F, TTCCAGTGGATG-GGCTGAAAAATC; AR-5R, ACGCGTTCTTCACTGTGTGTGGAAAT-AGATGGGCTTGACTTTGCCAGAAAGGATCTTGGGCACTTG; AR-3F, TTTGGAAACCCTAATACCC; AR-3R, CAAAGAGTCAGACCTTTCC. A point mutation was added by the AR-5R primer at gRNA PAM to prevent gRNA cutting donor DNA. C57BL/6J mice (4-6 weeks old) were used for zygote collection. CD1 females were used for injected embryo recipients. Guide RNA, CAS9 protein and donor DNA were mixed before injection into mouse zygotes at a final concentration of 5 µg/µl gRNA, 15 µg/µl CAS9 protein and 3 ng/µl dDNA. Injected zygotes were implanted into CD1 foster mothers. The genomic DNA samples were isolated from the offspring and analyzed by genomic PCR and DNA sequencing. Confirmed *Ar*$^{IRES\text{-}Cre}$ founder mice were then backcrossed with wild-type C57BL/6J for two to three generations to delete mosaicism resulting from Crispr/CAS9-based gene-editing approaches in mice.

Histology, immunostaining and mT/mG assays

Mouse tissues were fixed in 10% neutral-buffered formalin (American Master Tech Scientific) and processed in paraffin or processed to OCT following cryo-protection in 30% sucrose in 1× PBS (pH 7.3) at 4°C overnight as previously described (Lee et al., 2015). Following embedding in paraffin wax or OCT, tissue blocks were cut to 4 µm and 5 µm serial sections, respectively, and used for Hematoxylin and Eosin staining for further histological analysis (Lee et al., 2015). Immunohistochemistry was performed as previously described (Lee et al., 2015). In brief, tissue sections were rehydrated through a decreasing ethanol gradient. Heat-induced epitope retrieval was performed using a microwave to boil slides in 0.01 M citrate buffer (pH 6.0) followed by 15 min in 0.3% H_2O_2 in methanol. Next, tissue sections underwent blocking for 1 h at room temperature in 5% goat serum in 1× PBS (pH 7.3) followed by incubation with primary antibodies in 1% goat serum in PBS overnight at 4°C. Tissue sections were then washed with PBS and incubated with streptavidin ligated to horseradish peroxidase (Strep-HRP) (SA-5004, Vector Laboratories, 1:500 dilution) for 30 min and developed with 3,3′-diaminobenzidine (DAB) kit (SK-4100, Vector Laboratories). Tissue sections were counterstained in 5% Harris Hematoxylin and dehydrated through an increasing ethanol gradient. Coverslips were mounted using Permount Medium (SP15-500, Fisher Scientific).

Immunofluorescence staining was performed using similar procedures as described for immunohistochemistry; however, the use of H_2O_2 in methanol was excluded. Slides were developed with fluorescence-conjugated secondary antibodies and then mounted with coverslips using Vectashield Mounting Medium with DAPI (H-1200, Vector Laboratories). For detecting membrane-bound Tomato (mT) and membrane-bound green fluorescent protein (mGFP) signal, the staining was performed as previously described (Lee et al., 2015). Briefly, sections from the OCT-embedded tissues were washed with PBS (pH 7.30) and were developed with Vectashield Mounting Medium with DAPI (H-1200, Vector Laboratories). Antibodies used for both immunohistochemistry and immunofluorescence are listed in Table S5.

Microscope image acquisition

Images of Hematoxylin and Eosin and immunohistochemistry were acquired on an Axio Lab A1 microscope using 5×, 10×, 20× and 40× Zeiss A-Plan objectives with a Canon EOS 1000D camera and using Axiovision software (Carl Zeiss). Images of immunofluorescent staining and mTmG signals were acquired on a Nikon ECLIPSE E800 Epi-Fluorescence Microscope using 20× and 40× Nikon Plan Fluor objectives with a QImaging RETIGA EXi camera and using QCapture software (QImaging).

Single-cell RNA sequencing analysis

Female mice were placed with males overnight for mating, with the following day considered embryonic day (E) 0.5 if a vaginal plug was detected. Two individual sets of sc-RNA-seq experiments were performed using different littermates in this study. The urogenital sinuses of embryos were isolated at E17.5 and placed in DMEM with 10% FBS, 10 nM DHT, 5% Nuserum and 25 µg/ml insulin. The UGS was separated from the bladder at the bladder neck, and distal regions of the urethra and Wolffian ducts were removed (Fig. 2C). Once trimmed, UGS tissues were dissociated to single cells by digestion using 1 mg/mg collagenase at 37°C for 90 min and TrypLE (Gibco) at 37°C for 15 min. Approximately 11,000 viable cells obtained from male *R26R*$^{mTmG/+}$:*Ar*$^{IRES\text{-}Cre}$ embryos (n=4) were used for sequencing. Library preparation was performed using 10× Genomics Chromium Single Cell 3′ Solution with v3 chemistry following the manufacturer's protocol (10x Genomics). The library purity and size was validated by capillary electrophoresis using 2100 Bioanalyzer (Agilent Technologies). The library quantity was measured fluorometrically using Qubit dsDNA HS Assay Kit from Invitrogen. The libraries were sequenced with a NovaSeq 6000 instrument (Illumina) to a depth of ~130K reads per cell. Raw sequencing data were processed using the 10× Genomics' Cell Ranger pipeline (version 3.1.0) to generate FASTQ files and aligned to the mm10 genome with an added mGFP sequence (Zhang et al., 1996) to generate gene expression counts. Following alignment and initial quality control, a filtered feature bar coded matrix, including a total of 10,478 cells, was uploaded to R (3.6.1) using the Seurat package (3.1.3.9002) (Butler et al., 2018). Cells then underwent further filtering to remove potential empty droplets and doublets (1000<nFeature_RNA<9000) as well as low-quality cells with high percentages of mitochondrial RNA (percent.mt<15) (Fig. S1A,B). After this final filtering step, 9440 cells with an average of 4976 genes per cell and 31,214 UMI counts per cell were used for future analyses. Two individual sets of sc-RNA-seq experiments were performed using different littermates in this study.

For the visualization and analysis of scRNAseq results, normalized and scaled data were clustered using the top significant principal components (30) of 3000 highly variable genes with a resolution of 0.5 using Seurat (Fig. S1C,D). Trajectory analysis and generation of pseudotime was performed by converting Seurat objects into CellDataSet format. Following conversion of the data to a CellDataSet, trajectory analysis was performed using the Monocle2 package (2.12.0) (Qiu et al., 2017) in R. Identification of stem/progenitor populations was supported through the use of CytoTRACE (https://cytotrace.stanford.edu/) (Gulati et al., 2020). Interactome (ligand-receptor) analysis and visualization were performed using the SingleCellSignalR package (0.0.1.6) in R (Cabello-Aguilar et al., 2020). Pathway analysis was performed using Gene Set Enrichment Analysis (GSEA 4.0.3). Last, single-cell upstream regulator analysis was performed using Ingenuity Pathway Analysis (Qiagen, Version 51963813) and the SCENIC package (1.1.2.2) in R (Aibar et al., 2017).

Development (2021) 148, dev196048. doi:10.1242/dev.196048

Chromatin immunoprecipitation assay and qRT-PCR

The urogenital sinuses of embryos were isolated at E17.5. Mouse urogenital sinus mesenchyme (UGM) tissues were collected as reported previously (Xin et al., 2003). Briefly, the UGS was collected in 10 ml DMEM 10% FBS and 10 nM DHT, and rostral and caudal parts of UGS tissues and the Wolffian duct were removed. Trypsin was removed carefully, and digestion was stopped with 250 µl of DMEM, 20% FBS and 10 nM DHT followed by two washes with same amount of medium. The digested UGS was separated to UGE and UGM using a fine needle under a microscope. Mouse UGM (n=6) tissues were minced and incubated with 1% formaldehyde for 15 min and quenched with 0.150 M glycine for 10 min. Samples were washed sequentially with ice-cold PBS, and resuspended in cell lysis buffer [50 mM Tris-HCl (pH 8.0), 140 mM NaCl, 1 mM EDTA, 10% glycerol, 0.5% NP-40 and 0.25% Triton X-100], and then homogenized. The chromatin was sheared in nuclear lysis buffer [10 mM Tris-HCl (pH 8.0), 1 mM EDTA, 0.5 mM EGTA and 0.2% SDS] to an average size of 200-500 bp by sonication, diluted threefold in ChIP dilution buffer [0.01% SDS, 1.1% Triton X-100, 1.2 mM EDTA, 16.7 mM Tris-HCl (pH 8.1) and 167 mM NaCl], and then subjected to immunoprecipitation by magnetic protein G beads (Invitrogen) conjugated with AR (ab74272, Abcam). Crosslinks were reversed and chromatin DNA fragments were analyzed by real-time qPCR with specific primers (Table S6).

Statistical analysis

Differentially expressed gene lists were determined using a Wilcoxon Rank Sum test, with changes in expression at P<0.05 defined as significant. As recommended by the GSEA User Guide, pathways with FDR<0.25 were considered significant in exploratory GSEA pathway analysis. Source data underlying Figs 3D, 7B,C,D,F are provided in Tables S7-S11, respectively.

Competing interests

The authors declare no competing or financial interests.

Author contributions

Conceptualization: A.W.O., Z.S.; Methodology: D.-H.L., A.W.O., J.W., W.K.K., J.M., H.Z., V.L., A.H., X.W., Z.S.; Software: X.W.; Validation: D.-H.L., J.W., W.K.K., J.M., V.L., J.A., X.W., Z.S.; Formal analysis: A.W.O., Z.S.; Investigation: D.-H.L., A.W.O., J.W., J.M., H.Z., V.L., A.H., Z.S.; Resources: H.Z., J.A., Z.S.; Writing - original draft: A.W.O., Z.S.; Writing - review & editing: D.-H.L., A.W.O., J.W., J.A., Z.S.; Visualization: Z.S.; Supervision: Z.S.; Project administration: Z.S.; Funding acquisition: Z.S.

Funding

This work was supported by the National Institutes of Health (R01CA070297, R01CA166894 and R01DK104941 to Z.S.). Deposited in PMC for release after 12 months.

Data availability

The single-cell mRNA sequencing raw data have been deposited in GEO under accession number GSE153701.

Supplementary information

Supplementary information available online at
https://dev.biologists.org/lookup/doi/10.1242/dev.196048.supplemental

References

Abler, L. L., Keil, K. P., Mehta, V., Joshi, P. S., Schmitz, C. T. and Vezina, C. M. (2011). A high-resolution molecular atlas of the fetal mouse lower urogenital tract. *Dev. Dyn.* **240**, 2364-2377. doi:10.1002/dvdy.22730

Aibar, S., González-Blas, C. B., Moerman, T., Huynh-Thu, V. A., Imrichova, H., Hulselmans, G., Rambow, F., Marine, J.-C., Geurts, P., Aerts, J. et al. (2017). SCENIC: single-cell regulatory network inference and clustering. *Nat. Methods* **14**, 1083-1086. doi:10.1038/nmeth.4463

Aytes, A., Mitrofanova, A., Kinkade, C. W., Lefebvre, C., Lei, M., Phelan, V., LeKaye, H. C., Koutcher, J. A., Cardiff, R. D., Califano, A. et al. (2013). ETV4 promotes metastasis in response to activation of PI3-kinase and Ras signaling in a mouse model of advanced prostate cancer. *Proc. Natl. Acad. Sci. USA* **110**, E3506-E3515. doi:10.1073/pnas.1303558110

Bhatia-Gaur, R., Donjacour, A. A., Sciavolino, P. J., Kim, M., Desai, N., Young, P., Norton, C. R., Gridley, T., Cardiff, R. D., Cunha, G. R. et al. (1999). Roles for Nkx3.1 in prostate development and cancer. *Genes Dev.* **13**, 966-977. doi:10.1101/gad.13.8.966

Brun, J., Lutz, K. A., Neumayer, K. M. H., Klein, G., Seeger, T., Uynuk-Ool, T., Wörgötter, K., Schmid, S., Kraushaar, U., Guenther, E. et al. (2015). Smooth muscle-like cells generated from human mesenchymal stromal cells display marker gene expression and electrophysiological competence comparable to bladder smooth muscle cells. *PLoS ONE* **10**, e0145153. doi:10.1371/journal.pone.0145153

Butler, A., Hoffman, P., Smibert, P., Papalexi, E. and Satija, R. (2018). Integrating single-cell transcriptomic data across different conditions, technologies, and species. *Nat. Biotechnol.* **36**, 411-420. doi:10.1038/nbt.4096

Cabello-Aguilar, S., Alame, M., Kon-Sun-Tack, F., Fau, C., Lacroix, M. and Colinge, J. (2020). SingleCellSignalR: inference of intercellular networks from single-cell transcriptomics. *Nucleic Acids Res.* **48**, e55. doi:10.1093/nar/gkaa183

Chang, C. S., Kokontis, J. and Liao, S. T. (1988). Molecular cloning of human and rat complementary DNA encoding androgen receptors. *Science* **240**, 324-326. doi:10.1126/science.3353726

Chen, C., Zhang, Q., Liu, S., Parajuli, K. R., Qu, Y., Mei, J., Chen, Z., Zhang, H., Khismatullin, D. B. and You, Z. (2015). IL-17 and insulin/IGF1 enhance adhesion of prostate cancer cells to vascular endothelial cells through CD44-VCAM-1 interaction. *Prostate* **75**, 883-895. doi:10.1002/pros.22971

Cooke, P. S., Young, P. and Cunha, G. R. (1991). Androgen receptor expression in developing male reproductive organs. *Endocrinology* **128**, 2867-2873. doi:10.1210/endo-128-6-2867

Costantini, F. (2010). GDNF/Ret signaling and renal branching morphogenesis: from mesenchymal signals to epithelial cell behaviors. *Organogenesis* **6**, 252-262. doi:10.4161/org.6.4.12680

Crocoll, A., Zhu, C. C., Cato, A. C. B. and Blum, M. (1998). Expression of androgen receptor mRNA during mouse embryogenesis. *Mech. Dev.* **72**, 175-178. doi:10.1016/S0925-4773(98)00007-0

Cunha, G. R. (1984). Androgenic effects upon prostatic epithelium are mediated via trophic influences from stroma. *Prog. Clin. Biol. Res.* **145**, 81-102.

Cunha, G. R. and Chung, L. W. K. (1981). Stromal-epithelial interactions—I. Induction of prostatic phenotype in urothelium of testicular feminized (Tfm/y) mice. *J. Steroid. Biochem.* **14**, 1317-1324. doi:10.1016/0022-4731(81)90338-1

Cunha, G. R. and Lung, B. (1978). The possible influence of temporal factors in androgenic responsiveness of urogenital tissue recombinants from wild-type and androgen-insensitive (Tfm) mice. *J. Exp. Zool.* **205**, 181-193. doi:10.1002/jez.1402050203

Cunha, G. R., Donjacour, A. A., Cooke, P. S., Mee, S., Bigsby, R. M., Higgins, S. J. and Sugimura, Y. (1987). The endocrinology and developmental biology of the prostate. *Endocr. Rev.* **8**, 338-362. doi:10.1210/edrv-8-3-338

Cunha, G. R., Vezina, C. M., Isaacson, D., Ricke, W. A., Timms, B. G., Cao, M., Franco, O. and Baskin, L. S. (2018). Development of the human prostate. *Differentiation* **103**, 24-45. doi:10.1016/j.diff.2018.08.005

De Gendt, K., Swinnen, J. V., Saunders, P. T. K., Schoonjans, L., Dewerchin, M., Devos, A., Tan, K., Atanassova, N., Claessens, F., Lecureuil, C. et al. (2004). A Sertoli cell-selective knockout of the androgen receptor causes spermatogenic arrest in meiosis. *Proc. Natl. Acad. Sci. USA* **101**, 1327-1332. doi:10.1073/pnas.0308114100

Fontijn, R. D., Favre, J., Naaijkens, B. A., Meinster, E., Paauw, N. J., Ragghoe, S. L., Nauta, T. D., van den Broek, M. A., Weijers, E. M., Niessen, H. W. et al. (2014). Adipose tissue-derived stromal cells acquire endothelial-like features upon reprogramming with SOX18. *Stem Cell Res.* **13**, 367-378. doi:10.1016/j.scr.2014.09.004

Ganassi, M., Badodi, S., Ortuste Quiroga, H. P., Zammit, P. S., Hinits, Y. and Hughes, S. M. (2018). Myogenin promotes myocyte fusion to balance fibre number and size. *Nat. Commun.* **9**, 4232. doi:10.1038/s41467-018-06583-6

Gelmann, E. P. (2002). Molecular biology of the androgen receptor. *J. Clin. Oncol.* **20**, 3001-3015. doi:10.1200/JCO.2002.10.018

Georgas, K. M., Armstrong, J., Keast, J. R., Larkins, C. E., McHugh, K. M., Southard-Smith, E. M., Cohn, M. J., Batourina, E., Dan, H., Schneider, K. et al. (2015). An illustrated anatomical ontology of the developing mouse lower urogenital tract. *Development* **142**, 1893-1908. doi:10.1242/dev.117903

Goscinski, M. A., Xu, R., Zhou, F., Wang, J., Yang, H., Huang, R., Li, Y., Larsen, S. G., Giercksky, K.-E., Nesland, J. M. et al. (2015). Nuclear, cytoplasmic, and stromal expression of ZEB1 in squamous and small cell carcinoma of the esophagus. *APMIS* **123**, 1040-1047. doi:10.1111/apm.12473

Grishina, I. B., Kim, S. Y., Ferrara, C., Makarenkova, H. P. and Walden, P. D. (2005). BMP7 inhibits branching morphogenesis in the prostate gland and interferes with Notch signaling. *Dev. Biol.* **288**, 334-347. doi:10.1016/j.ydbio.2005.08.018

Guerrero-Juarez, C. F., Dedhia, P. H., Jin, S., Ruiz-Vega, R., Ma, D., Liu, Y., Yamaga, K., Shestova, O., Gay, D. L., Yang, Z. et al. (2019). Single-cell analysis reveals fibroblast heterogeneity and myeloid-derived adipocyte progenitors in murine skin wounds. *Nat. Commun.* **10**, 650. doi:10.1038/s41467-018-08247-x

Gulati, G. S., Sikandar, S. S., Wesche, D. J., Manjunath, A., Bharadwaj, A., Berger, M. J., Ilagan, F., Kuo, A. H., Hsieh, R. W., Cai, S. et al. (2020). Single-cell transcriptional diversity is a hallmark of developmental potential. *Science* **367**, 405-411. doi:10.1126/science.aax0249

Habuka, M., Fagerberg, L., Hallström, B. M., Pontén, F., Yamamoto, T. and Uhlen, M. (2015). The urinary bladder transcriptome and proteome defined by transcriptomics and antibody-based profiling. *PLoS ONE* **10**, e0145301. doi:10.1371/journal.pone.0145301

Henry, G. H., Malewska, A., Joseph, D. B., Malladi, V. S., Lee, J., Torrealba, J., Mauck, R. J., Gahan, J. C., Raj, G. V., Roehrborn, C. G. et al. (2018). A cellular anatomy of the normal adult human prostate and prostatic urethra. *Cell Rep.* **25**, 3530-3542.e5. doi:10.1016/j.celrep.2018.11.086

Herriges, J. C., Verheyden, J. M., Zhang, Z., Sui, P., Zhang, Y., Anderson, M. J., Swing, D. A., Zhang, Y., Lewandoski, M. and Sun, X. (2015). FGF-regulated ETV transcription factors control FGF-SHH feedback loop in lung branching. *Dev. Cell* **35**, 322-332. doi:10.1016/j.devcel.2015.10.006

Huang, L., Pu, Y., Hu, W. Y., Birch, L., Luccio-Camelo, D., Yamaguchi, T. and Prins, G. S. (2009). The role of Wnt5a in prostate gland development. *Dev. Biol.* **328**, 188-199. doi:10.1016/j.ydbio.2009.01.003

Iber, D. and Menshykau, D. (2013). The control of branching morphogenesis. *Open Biol* **3**, 130088. doi:10.1098/rsob.130088

Jacob, C., Lotscher, P., Engler, S., Baggiolini, A., Varum Tavares, S., Brugger, V., John, N., Buchmann-Moller, S., Snider, P. L., Conway, S. J. et al. (2014). HDAC1 and HDAC2 control the specification of neural crest cells into peripheral glia. *J. Neurosci.* **34**, 6112-6122. doi:10.1523/JNEUROSCI.5212-13.2014

Javed, S. and Langley, S. E. M. (2014). Importance of HOX genes in normal prostate gland formation, prostate cancer development and its early detection. *BJU Int.* **113**, 535-540. doi:10.1111/bju.12269

Jenster, G., van der Korput, H. A. G. M., van Vroonhoven, C., van der Kwast, T. H., Trapman, J. and Brinkmann, A. O. (1991). Domains of the human androgen receptor involved in steroid binding, transcriptional activation, and subcellular localization. *Mol. Endocrinol.* **5**, 1396-1404. doi:10.1210/mend-5-10-1396

Jessen, K. R. and Mirsky, R. (2005). The origin and development of glial cells in peripheral nerves. *Nat. Rev. Neurosci.* **6**, 671-682. doi:10.1038/nrn1746

Kanamori-Katayama, M., Kaiho, A., Ishizu, Y., Okamura-Oho, Y., Hino, O., Abe, M., Kishimoto, T., Sekihara, H., Nakamura, Y., Suzuki, H. et al. (2011). LRRN4 and UPK3B are markers of primary mesothelial cells. *PLoS ONE* **6**, e25391. doi:10.1371/journal.pone.0025391

Karpus, O. N., Westendorp, B. F., Vermeulen, J. L. M., Meisner, S., Koster, J., Muncan, V., Wildenberg, M. E. and van den Brink, G. R. (2019). Colonic CD90+ crypt fibroblasts secrete semaphorins to support epithelial growth. *Cell Rep.* **26**, 3698-3708.e5. doi:10.1016/j.celrep.2019.02.101

Keil, K. P., Mehta, V., Branam, A. M., Abler, L. L., Buresh-Stiemke, R. A., Joshi, P. S., Schmitz, C. T., Marker, P. C. and Vezina, C. M. (2012). Wnt inhibitory factor 1 (Wif1) is regulated by androgens and enhances androgen-dependent prostate development. *Endocrinology* **153**, 6091-6103. doi:10.1210/en.2012-1564

Komar, A. A. and Hatzoglou, M. (2011). Cellular IRES-mediated translation: the war of ITAFs in pathophysiological states. *Cell Cycle* **10**, 229-240. doi:10.4161/cc.10.2.14472

Kwon, O.-J., Zhang, Y., Li, Y., Wei, X., Zhang, L., Chen, R., Creighton, C. J. and Xin, L. (2019). Functional heterogeneity of mouse prostate stromal cells revealed by single-cell RNA-seq. *iScience* **13**, 328-338. doi:10.1016/j.isci.2019.02.032

Le, V., He, Y., Aldahl, J., Hooker, E., Yu, E.-J., Olson, A., Kim, W. K., Lee, D.-H., Wong, M., Sheng, R. et al. (2020). Loss of androgen signaling in mesenchymal sonic hedgehog responsive cells diminishes prostate development, growth, and regeneration. *PLoS Genet.* **16**, e1008588. doi:10.1371/journal.pgen.1008588

Lee, D.-K., Liu, Y., Liao, L., Wang, F. and Xu, J. (2014). The prostate basal cell (BC) heterogeneity and the p63-positive BC differentiation spectrum in mice. *Int. J. Biol. Sci.* **10**, 1007-1017. doi:10.7150/ijbs.9997

Lee, S. H., Johnson, D. T., Luong, R., Yu, E. J., Cunha, G. R., Nusse, R. and Sun, Z. (2015). Wnt/β-catenin-responsive cells in prostatic development and regeneration. *Stem Cells* **33**, 3356-3367. doi:10.1002/stem.2096

Lu, B. C., Cebrian, C., Chi, X., Kuure, S., Kuo, R., Bates, C. M., Arber, S., Hassell, J., MacNeil, L., Hoshi, M. et al. (2009). Etv4 and Etv5 are required downstream of GDNF and Ret for kidney branching morphogenesis. *Nat. Genet.* **41**, 1295-1302. doi:10.1038/ng.476

Madison, B. B., McKenna, L. B., Dolson, D., Epstein, D. J. and Kaestner, K. H. (2009). FoxF1 and FoxL1 link hedgehog signaling and the control of epithelial proliferation in the developing stomach and intestine. *J. Biol. Chem.* **284**, 5936-5944. doi:10.1074/jbc.M808103200

Muzumdar, M. D., Tasic, B., Miyamichi, K., Li, L. and Luo, L. (2007). A global double-fluorescent Cre reporter mouse. *Genesis* **45**, 593-605. doi:10.1002/dvg.20335

Narlis, M., Grote, D., Gaitan, Y., Boualia, S. K. and Bouchard, M. (2007). Pax2 and pax8 regulate branching morphogenesis and nephron differentiation in the developing kidney. *J. Am. Soc. Nephrol.* **18**, 1121-1129. doi:10.1681/ASN.2006070739

Nash, C., Boufaied, N., Badescu, D., Wang, Y. C., Paliouras, M., Trifiro, M., Ragoussis, I. and Thomson, A. A. (2019). Genome-wide analysis of androgen receptor binding and transcriptomic analysis in mesenchymal subsets during prostate development. *Dis. Model. Mech.* **12**, dmm039297. doi:10.1242/dmm.039297

Ochoa-Espinosa, A. and Affolter, M. (2012). Branching morphogenesis: from cells to organs and back. *Cold Spring Harb. Perspect. Biol.* **4**, a008243. doi:10.1101/cshperspect.a008243

Pellecchia, A., Pescucci, C., De Lorenzo, E., Luceri, C., Passaro, N., Sica, M., Notaro, R. and De Angioletti, M. (2012). Overexpression of ETV4 is oncogenic in prostate cells through promotion of both cell proliferation and epithelial to mesenchymal transition. *Oncogenesis* **1**, e20. doi:10.1038/oncsis.2012.20

Podlasek, C. A., Barnett, D. H., Clemens, J. Q., Bak, P. M. and Bushman, W. (1999). Prostate development requires Sonic hedgehog expressed by the urogenital sinus epithelium. *Dev. Biol.* **209**, 28-39. doi:10.1006/dbio.1999.9229

Prins, G. S. and Putz, O. (2008). Molecular signaling pathways that regulate prostate gland development. *Differentiation* **76**, 641-659. doi:10.1111/j.1432-0436.2008.00277.x

Qiu, X., Mao, Q., Tang, Y., Wang, L., Chawla, R., Pliner, H. A. and Trapnell, C. (2017). Reversed graph embedding resolves complex single-cell trajectories. *Nat. Methods* **14**, 979-982. doi:10.1038/nmeth.4402

Shah, N. M., Pisapia, D. J., Maniatis, S., Mendelsohn, M. M., Nemes, A. and Axel, R. (2004). Visualizing sexual dimorphism in the brain. *Neuron* **43**, 313-319. doi:10.1016/j.neuron.2004.07.008

Spaderna, S., Schmalhofer, O., Hlubek, F., Berx, G., Eger, A., Merkel, S., Jung, A., Kirchner, T. and Brabletz, T. (2006). A transient, EMT-linked loss of basement membranes indicates metastasis and poor survival in colorectal cancer. *Gastroenterology* **131**, 830-840. doi:10.1053/j.gastro.2006.06.016

Staack, A., Donjacour, A. A., Brody, J., Cunha, G. R. and Carroll, P. (2003). Mouse urogenital development: a practical approach. *Differentiation* **71**, 402-413. doi:10.1046/j.1432-0436.2003.7107004.x

Takeda, H. and Chang, C. (1991). Immunohistochemical and *in-situ* hybridization analysis of androgen receptor expression during the development of the mouse prostate gland. *J. Endocrinol.* **129**, 83-89. doi:10.1677/joe.0.1290083

Thomson, A. A., Timms, B. G., Barton, L., Cunha, G. R. and Grace, O. C. (2002). The role of smooth muscle in regulating prostatic induction. *Development* **129**, 1905-1912.

Toivanen, R., Mohan, A. and Shen, M. M. (2016). Basal progenitors contribute to repair of the prostate epithelium following induced luminal anoikis. *Stem Cell Rep.* **6**, 660-667. doi:10.1016/j.stemcr.2016.03.007

Varner, V. D. and Nelson, C. M. (2014). Cellular and physical mechanisms of branching morphogenesis. *Development* **141**, 2750-2759. doi:10.1242/dev.104794

Wang, X., Xu, H., Cheng, C., Ji, Z., Zhao, H., Sheng, Y., Li, X., Wang, J., Shu, Y., He, Y. et al. (2020). Identification of a Zeb1 expressing basal stem cell subpopulation in the prostate. *Nat. Commun.* **11**, 706. doi:10.1038/s41467-020-14296-y

Xie, T., Wang, Y., Deng, N., Huang, G., Taghavifar, F., Geng, Y., Liu, N., Kulur, V., Yao, C., Chen, P. et al. (2018). Single-cell deconvolution of fibroblast heterogeneity in mouse pulmonary fibrosis. *Cell Rep.* **22**, 3625-3640. doi:10.1016/j.celrep.2018.03.010

Xin, L., Ide, H., Kim, Y., Dubey, P. and Witte, O. N. (2003). In vivo regeneration of murine prostate from dissociated cell populations of postnatal epithelia and urogenital sinus mesenchyme. *Proc. Natl. Acad. Sci. USA* **100**, 11896-11903. doi:10.1073/pnas.1734139100

Yu, M., Gipp, J., Yoon, J. W., Iannaccone, P., Walterhouse, D. and Bushman, W. (2009). Sonic hedgehog-responsive genes in the fetal prostate. *J. Biol. Chem.* **284**, 5620-5629. doi:10.1074/jbc.M809172200

Zhang, G., Gurtu, V. and Kain, S. R. (1996). An enhanced green fluorescent protein allows sensitive detection of gene transfer in mammalian cells. *Biochem. Biophys. Res. Commun.* **227**, 707-711. doi:10.1006/bbrc.1996.1573

Zhang, L., Zhang, B., Han, S. J., Shore, A. N., Rosen, J. M., Demayo, F. J. and Xin, L. (2012). Targeting CreER(T2) expression to keratin 8-expressing murine simple epithelia using bacterial artificial chromosome transgenesis. *Transgenic Res.* **21**, 1117-1123. doi:10.1007/s11248-012-9598-y

Zhang, Y., Yokoyama, S., Herriges, J. C., Zhang, Z., Young, R. E., Verheyden, J. M. and Sun, X. (2016). E3 ubiquitin ligase RFWD2 controls lung branching through protein-level regulation of ETV transcription factors. *Proc. Natl. Acad. Sci. USA* **113**, 7557-7562. doi:10.1073/pnas.1603310113